# Structural and chemical change of graphene

Jong-Chul Yoon

Department of Chemical Engineering

Graduate School of UNIST

# Structural and chemical change of graphene

A thesis/dissertation
submitted to the Graduate School of UNIST
in partial fulfillment of the
requirements for the degree of
Master of Science

Jong-Chul Yoon

6. 05. 2017

Approved by

Advisor
Ji-Hyun Jang

# Structural and chemical change of graphene

Jong-Chul Yoon

This certifies that the thesis/dissertation of Jong-Chul Yoon is approved.

6. 05. 2017

signature

Advisor: Ji-Hyun Jang

signature

Jin Young Kim

signature

Hyun-Kon Song

**Table of contents**

LIST OF FIGURE

LIST OF TABLE

**ABSTRACT**

Graphene has attractive great attention from many scientists due to its supernal properties such as electrical, thermal, optical, chemical, mechanical properties. Since 2004, many methods to make graphene had investigated such as epitaxial growth, chemical vapor deposition. Graphene has advantages that can be applied to many fields and research is under way to further strengthen it. One of them is to convert the two-dimensional graphene into a three-dimensional structure. Three-dimensional (3D) structured graphene not only preserves the existing advantages, but also has a large surface area to avoid re-stacking. Another way is to modify the surface to activate the surface of graphene. First, I studied on the route to make 3D graphene and lotus leaf-inspired 3D graphene using CVD methods and the change of graphene surface with different transfer method and its used as SERS substrate. To fabricate 3D structured graphene, we employed silica particle as template and the prepared 3D graphene used for super capacitor and We studied a method to directly fabricate lotus leaf-inspired 3-dimensional (3D) graphene structures by a CVD method. By simply heating commercial copper foil under an oxygen condition, CuO nanowhiskers supported on a copper substrate have been created. The annealing of CuO under a hydrogen condition at high temperature returns CuO (II) back to Cu (0), leading to reconstruction of the 3D structures in the form of double hierarchical bumps. The 3D graphene we have synthesized is assembled with properties similar to those of individual graphene sheet but possess an additional super-hydrophobic property obtained by the shape of the lotus leaf-inspired double hierarchical bumps. Second, we explore the effect of the method used to transfer the copper-foil-grown graphene onto another substrate on its chemical effect on the Raman scattering. We have found that graphene transferred using the PMMA method produces 6 times the RS signal increase of that produced by graphene transferred using thermal release. In addition, the large surface area and the availability of 3-dimensional responses to external stimuli provide further potential for using 3D structures in diverse areas of energy-related materials and tissue engineering. In particular, porous carbon materials have been suggested as effective electrodes for energy devices due to their large surface area and size tunable porosity for easy access of the electrolyte. More specifically, effective surface area and pore volume the nanostructure provide active sites for better performance of the energy devices, which operates via a mechanism of charge-transfer at the electrochemical interface between the electrode and electrolyte. Lastly, I studied on the direct route to producing hierarchical graphene structures of fertility-layer graphene grown by CVD without using flammable gas. Meso-pores are formed by the loss of organic materials during the carbonization process of polymer composites and metal precursors. Carbonized carbon and reduced metal precursors in a hierarchical structure formed by the thermal annealing of the sample in a hydrogen gas environment provide a solid carbon source and a catalyst for the graphene growth during the CVD process, respectively. The outstanding properties of

hierarchical graphene structures suggest the great potential of interconnected graphene networks for application.

# CHAPTER 1. REVIEW

## 1.1 Graphene

### 1.1.1 Introduction

Historically, carbon allotrope is attractive many scientist. Graphite (figure 1 a and b), the longest known carbon allotrope, was discovered in a nine near Borrowdale in the 16$^{th}$ century. Graphite is stacking of graphene sheets (figure 1 b) due to the van der Waals interaction which is weaker than covalent bonds. These properties explain why it is scratched over rough surface such as a paper. Thin layered graphene sheets are exfoliated from graphite and now stick to the surface because of weak van der Waals interaction between layers. In 1985, Robert Curl et al discovered 0-D graphitic allotrope named fullerenes[1]. It consists of a graphene sheet and forms graphene sphere because some hexagons in graphene are collapse and crumbling (figure 1c). C60 had been predicted before, in 1970, by Eiji Ozawa. Furthermore, Sumio Iijima introduced new carbon allotrope known as carbon nanotubes(CNT) (figure 1 d-e) which is 1D carbon material and rolled up graphene sheet with few nanometers diameter[2],. Lastly, in 2004, the graphene, a carbon sheet having atomic scale thickness including sp2-bonded carbon atoms in a honeycomb crystal lattice, has introduced by novoselov et al.[3] This finding is attractive large attention as materials for next generation because it has supernal properties such as electric properties, ballistic transport, thermal conductivity, optical property and chemical stability. The mechanical cleavage, which is first method to obtain a single graphene, gave high-quality graphene sheet and many scientists the opportunity to study natural properties of graphene[4]. Furthermore, this method led to new study field to grow graphene. Due to that, high-quality graphene produced using epitaxial growth and CVD method and new methods to transfer produced high-quality graphene to other substrate for application in devices[5] have introduced

### 1.1.2 Electronic properties

The pure graphene sheet has attractive electronic properties such as high charge-carrier mobility, am-bipolar field effect, quantum hall effects, ballistic transport and Klein paradox due to the 2D single atom thick hexagonal lattice[6-7]. The carrier mobility of free standing graphene on a substrate can reach up to 200,000 $cm^2V^{-1}S^{-1}$ which can use for ultrafast electronics and optoelectronics[8]. Unfortunately, however, its is limited up to 15,000 $cm^2V^{-1}S^{-1}$ because the ripples, scattering and defects are formed during growth and transfer[3,7]. Since graphene has a zero gap, a lot of science make efforts to open a band gap using different methods, such as 1D nanoribbon, nano-mesh and hydrogen patterning. However, because graphene has a zero band gap, many efforts have been tried to open a band gap such as ribbon 2D graphene, nano-mesh and patterning[9-11].

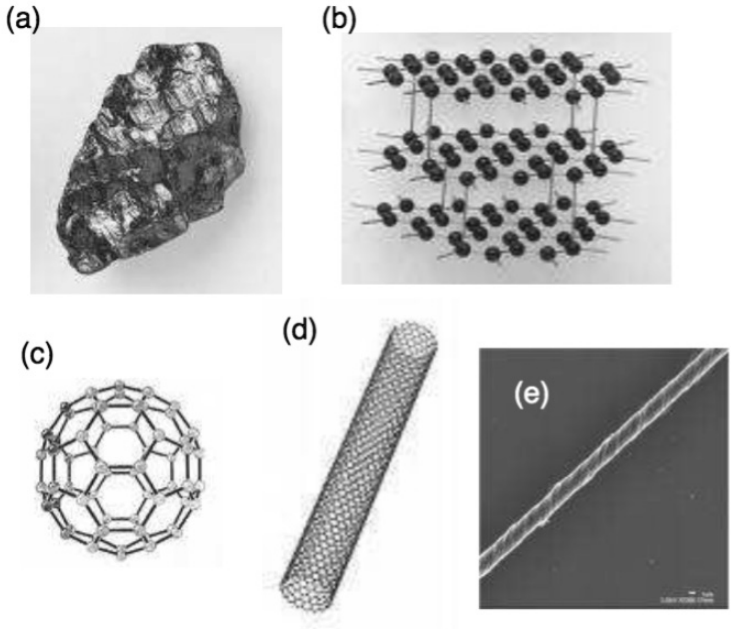


**Figure 1 : Graphitic allotopes (a)bulk Graphite. (b) Layered Structure of graphite. (c) 0-D allotope. (d) 1-D allotope : single-wall carbon nanotube. (e) Optical image of a carbon nanotube.**

### 1.1.3 Mechanical properties of graphene

The mechanical properties of pristine sheet have been determined using AFM (figure 2 a and b). The graphene without defect had a Young's modulus of up to 1.0 TPa and a fracture strength of 130 GPa[12]. Table 1 shows the experimental Young's moduli of graphene is from 0.9 to 1.1 TPa[12]. Many parameters that affect the Young's modulus of graphene, such as the chirality Young's the chirality[13], the presence of defects and wrinkles[14], and functionalization[15-16] had reported. Figure 2c indicates the model for graphene with armchair(zigzag) from 0 to 30º, showing that the Young's modulus varied in a narrow range from 1.0086 TPa (the zigzag) to 1.050 TPa (the armchair) (figure 2 d). This result approved with the previous theoretical elastic properties of graphene should be relatively independent of the orientation direction and thus the Young's modulus should not be affected by the chirality model.

### 1.1.4 Optical properties

The Dirac fermions of graphene (the infrared to visible light) is invariable and presented by the high-frequency conductivity of Dirac fermions in graphene is constant and given by

$$\pi e^2 / 2h. \qquad \text{eq 1}$$

For incidence light, T(indicates the optical transmittance) and R(reflectance) are given as follows:

$$T=(1+1/2\pi\alpha)^{-2} \qquad \text{eq 2}$$

$$R=(1/4)\pi^2\alpha^2 T, \qquad \text{eq 3}$$

where

$$\alpha= 2\pi e^2 / hc \approx 1/137 \qquad \text{eq 4}$$

*e* represents the electron charge, *c* and *h* is the light speed, and the Planck's constant. amalgamating Eqs. (3) and (4) yields the opacity of graphene:

$$(1-T) \approx \pi\alpha \approx 2.3\%. \qquad \text{eq 5}$$

According to figure 3 a-b, the transparency of mono-layer graphene is ~97.7%, and the opacity is linearly proportional with increasing the number of layers with one layer equivalent to 2.3 %[21].

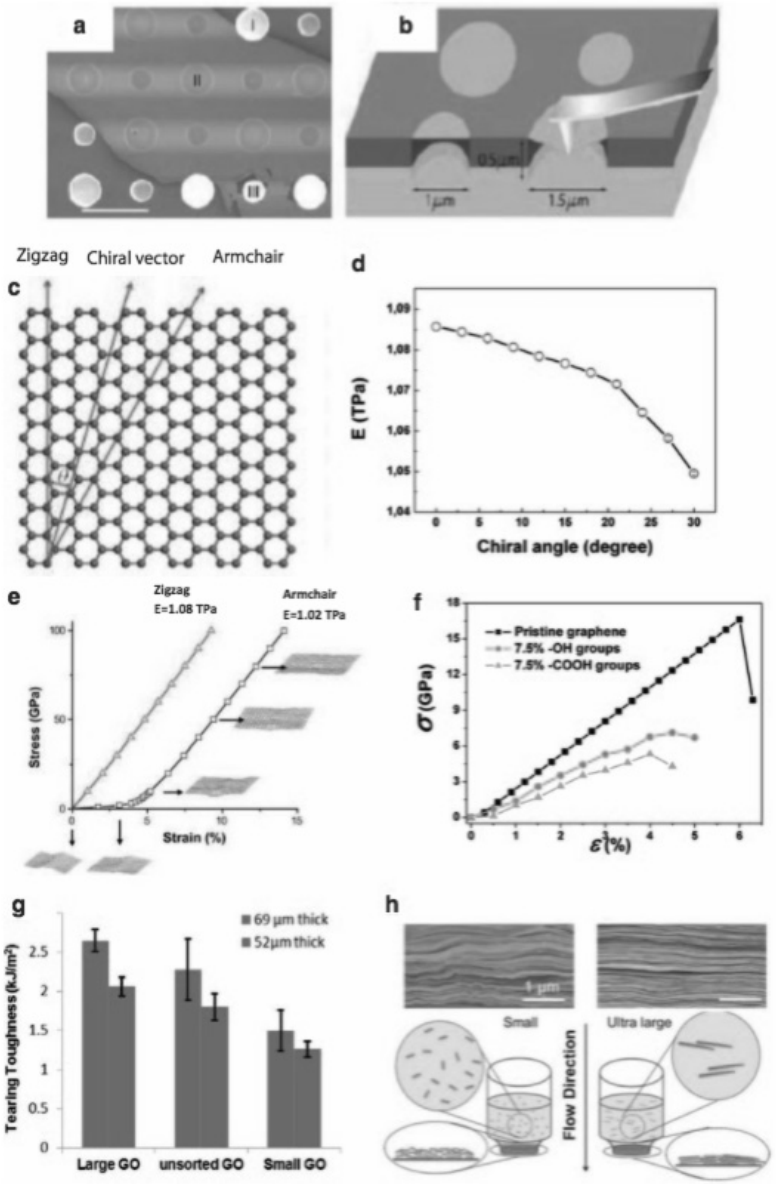


**Figure 2. Mechanical properties of graphene sheet, graphene oxide(GO), and GO papers. (a). SEM image of a graphene sheet. (b) Schematic of free standing graphene. (c) Molecular model of graphene with chiral angles[13]. (d) Young's modulus of graphene with different chiral angles[13]. (e) Stress-strain curve of graphene sheets containing stone-Wales defects along with morphological changes with increasing strain[14]. (f) Shear stress–strain curves for pristine graphene and GO sheets functionalized with carboxyl and hydroxyl groups[13]. (g) Tearing tough- ness of GO papers with different size groups[17]. (h) Cross-sectional SEM images and schematic of self-assembly process of GO sheets with different sizes[13] (S-GO in the left panel and UL-GO in the right panel). SEM scanning electron microscope, S-GO small graphene oxide, UL-GO ultra-large graphene oxide[3].**

| *Method*[13,15,16,18-20] | *E(TPa)* |
|---|---|
| *Nanoindentation* | 1.02 |
| *Phonon dispersion* | 1.01 |
| *Ab initio computations* | 1.05 |
| *Density functional theory* | 1.05 |
| *First principles calculations* | 1.01 |
| *MD and MM simulation* | 1.05-1.09 |
| *Empirical force constant calculations* | 1.13 |

**Table 1. Young's modulus of pristine graphene from representative experimental and theoretical investigation[18].**

These observations were further proven for CVD- graphene that the optical transmittance was reduced by 2.2–2.3% for an increasing number of layer [22](Figure. 2 (a)). Therefore, the thickness of graphene was determined using white light on samples supported on a $SiO_2$/Si substrate[23], as shown in Figure. 2(d).

### 1.1.5 Thermal properties

The thermal properties of lattice vibrations of graphene have attracted interest of researcher in the physics, chemical, material, and engineering part. Transport properties of graphene were substantially different compared to bulk graphite or 3D materials. Because the carrier density of natural graphene is relatively low, the electronic contribution in thermal conductivity of graphene should be negligible by the Wiedemann Franz law. The that of graphene is controlled by transport properties of phonon in graphene. Acoustic phonons of graphene are the major heat carriers at room temperature, whereas optical phonons are used for counting the number layers using Raman spectra with FLG[26]. The theoretical thermal conductivity of suspended monolayer graphene is about 6000 $Wm^{-1}K^{-1}$ at room temperature according to the MD simulations by the Green–Kubo approach. it is much higher than that of graphitic carbon[27]. The thermal conductivities of that were measured using an Raman spectra where a incident light was focused on a suspended graphene sheet over a 1-μm-wide trench, which was connected to heat sinks at its ends to provide heat sources. Thermal conductivities were determined from the dependence of Raman G-peak wavelength and the independently measured G-peak temperature coefficient. The thermal conductivity of single-layer graphene is from $4.84\times10^3$ to $5.30 \times 10^3$ W/mK at room temperature.

### 1.1.6 Synthesis methods

#### 1.1.6.1 Exfoliation and cleavage

Mechanical exfoliation is the interesting method to peel off single graphene from graphite flakes using simple item such as a Scotch tape. As shown in Figure. 3, the graphene was optically confirmed on $SiO_2$ layer on Si[3,4]. Since the van der Waals force between interlayers in graphite is very weak (inter-action energy of ~ 2 eV/nm[22]), it can be easily exfoliated by Scotch tape[28]. The graphene and graphite flake can be transferred onto the substrate having smooth surface and thin pieces using optical microscopy by the tape[3,29].

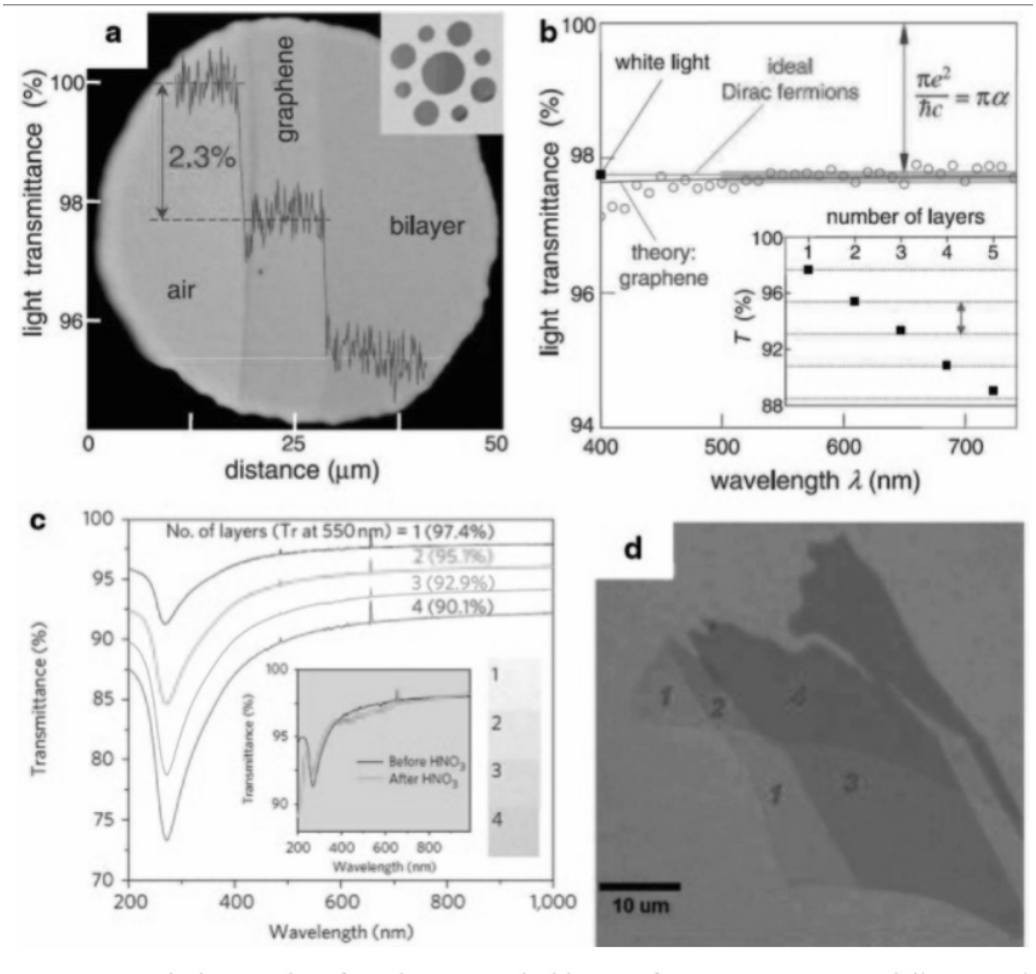


**Figure 3. Optical properties of graphene. (a). Optical image of monolayer and bilayer graphene sheets on the substrate. (b0 Transmittance of monolayer graphene (open circles). (Inset) Transmittance as a function of number of graphene layers. (c) UV–vis spectra of layered transferred graphene films on substrates. (d) Optical image of graphene with different layers[29]**

The method determinates skill to find mono-layer graphene sheets in multilayer flakes, and after likely number of graphene layers are identified with an optical microscope. Thicknesses of graphene layer can be determinated by Raman spectrum or AFM[29]. The choice of substrate is important and the apparent contrast of graphene monolayer on a $SiO_2$/Si substrate was up to 12 % at 550 nm. This finding was explained by a Fabry–Perot multilayer cavity. The optical path added by graphene to the interference of the $SiO_2$/Si substrate[30,31]. Thick graphite flakes deposited on a $SiO_2$ appeared yellow to bluish with decreasing the thickness (Fig. 3 (a)), while multi or mono-layer graphene appeared darker to lighter purple (Fig. 3 (b)). This skill is not scalable and for mass production, even though the samples of graphene thereby obtained should be useful to characterize inherent properties in fundamental studies.

#### 1.1.6.2 Thermal chemical vapor deposition

##### 1.1.6.2.1 Graphene grown on Ni

In case of Chemical Vapor Deposition(CVD) methods, graphene is grown directly on a transition metal surface using saturation of carbon with injection to a carbon precursor at a high temperature[5,22]. Nickel or copper films are common used to grow graphene as the substrate with the carbon source as gas. Once the temperature of substrate is decreased to room temperature, the melt carbon in metal on the substrate saturate and the carbon triggers to form one- to few-layer graphene sheets on the substrate. One of advantages of this method is their high compatibility with the CMOS (complementary metal oxide semiconductor) technology. A standard disadvantage is that controlling the film thickness is hard and poly-crystals are easily formed[33], although some methods has been succeeded to make equal graphene layers using the CVD method[34]. Another disadvantage is that substrate materials for graphene growth is expensive, significantly limiting its applications for large-scale production. Nevertheless, this method is an important to produce mass production with no defect and electronic disorder, making it an outstanding potential for applications. The formation of FLG on surface of metal has been known. In most cases, the Ni films with polycrystalline deposited on $SiO_2$/Si wafer are first annealed up to 1000 °C with $H_2$ and Ar gas to make smooth surface. The nickel films are then exposed to a $H_2$ and $CH_4$ mixture so that the carbon source was supplied and can dissolve into the Ni film due to high solubility of carbon at high temperature. Finally, the metal substrate is cooled down to room temperature in an inert mood. As the solubility of carbon atoms decreases as the temperature goes down, the carbon atoms saturate from the Ni–C solid solution during cooling and precipitate onto the Ni surface to form graphene films[35].

##### 1.1.6.2.2 Graphene on Cu

because of the solubility of carbon in metal and grain boundaries of metal surface, the grown graphene films usually form both one and multi-layer graphene with polycrystalline. Copper foil is a potentially suitable substrate to grow one layer or multi-layer graphene because Cu has extremely low solubility of carbon[37]. Ruoff's group first reported the methods to grow high-quality single-layer graphene on polycrystalline Cu foils, which attracted attention due to the advantages of good control of graphene

layers, low cost, and transfer. The Cu foil was annealed at 1000 °C in a hydrogen and argon atmosphere. A mixture of $H_2/CH_4$ gas was then injected into the chamber to make trigger of graphene and grow graphene on the Cu foil. The substrate was cooled down to room temperature in inert mood after a continuous graphene was formed. The SEM image clearly shows Cu grains with color contrast. The high-resolution SEM indicates that these Cu surface steps were formed during thermal annealing. The darker flakes indicate multilayer graphene, while the wrinkles originated from the different thermal expansion coefficients between graphene and Cu. The wrinkles went across the Cu grain boundaries, confirming that the graphene film was continuous. The grown graphene films can be transferred to another substrate using various transfer methods. The quality and uniformity were determined by Raman spectroscopy. The Raman spectra showed a G to 2D peak intensity ratio ($I_G/I_{2D}$) of ~ 0.5 and a symmetric 2D band centered at ~ 2680 $cm^{-1}$ with a full width at half maximum (FWHM) of ~ 33 $cm^{-1}$, confirming the monolayer graphene.

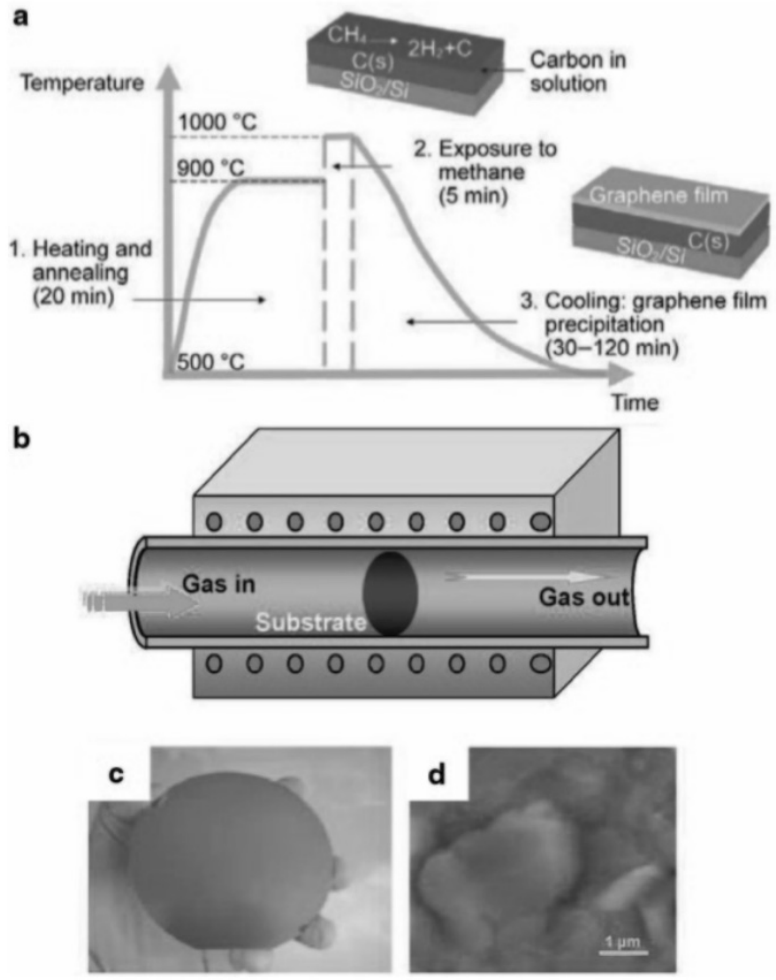


**Figure 4 :** Graphene on a nickel substrate. (A) Illustration of graphene growth in different steps. (B) Schematic of full-wafer scale deposition of graphene layers on polycrystalline Ni by chemical vapor deposition (CVD). (C) E-beam-evaporated Ni film of thickness 100 nm on a 10 cm diameter $SiO_2$/Si wafer. (D) Atomic force microscopy (AFM) image of a Ni film after CVD of graphene layers[35].

#### 1.2.6.1 Chemical methods

The most common methods for oxidation of graphite is using graphite powder, which allow produced by removing contaminations from naturally occurring graphite and mass production[38]. Because of the gap between inter-layers in graphite, the intercalating agents are able to expend between the graphene layers under chemical reactions, forming graphite intercalation compound (GIC). The experiments to investigate the insertion of additional chemical species between the basal planes have been performed extensively since the successful formation of the first intercalation compound using potassium[33]. Figure 5 shows the structures of GICs, which correspond to approximate compositions[39]. The interlayer spacing of GIC has increased from 0.34 nm to 1 nm depending on the intercalant with reducing the van der Waals forces between sheet. The weak van der Waals forces make easier to exfoliate graphene from graphite, offering a possible route to fabricate single layer graphene or graphene oxide (GO). Other methods is using expansion of interlayer spacing by thermal shock (~ 1000 °C) to produce expanded graphite (EG). As shown in Fig. 5, the halogen intercalants can be introduced into the host material of highly ordered pyrolytic graphite (HOPG) and sequentially to form layered structures[40].

Graphite oxide was first prepared almost 150 years ago by Brodie, who treated graphite repeatedly with potassium chlorate and nitric acid[9]. The oxidizing agent made negatively charged thin platelets form surface of graphite that consist of single- to multilayer carbon. Monolayer graphite oxide is now widely acknowledged and recognized as GO. The term “sheets” usually indicate monolayer to several layers, while “platelets” is often used to describe thicker multilayer GO or rGO[42]. Figure 5 shows the process involved in the exfoliation of graphite oxide into individual GO sheets. The exfoliation is facilitated by rapid heating or ultrasonic agitation, while excessive ultra-sonication often results in breakage or fragmentation along with a significant reduction in lateral dimensions of GO sheets[43]. Individual GO sheets can be viewed as graphene decorated with oxygenated functional groups on the basal plane and around the edges. Due to the ionization of carboxyl groups present at the edges, GO can be electrostatically stable to form a colloidal suspension in water, alcohols, and certain organic solvents without surfactants.

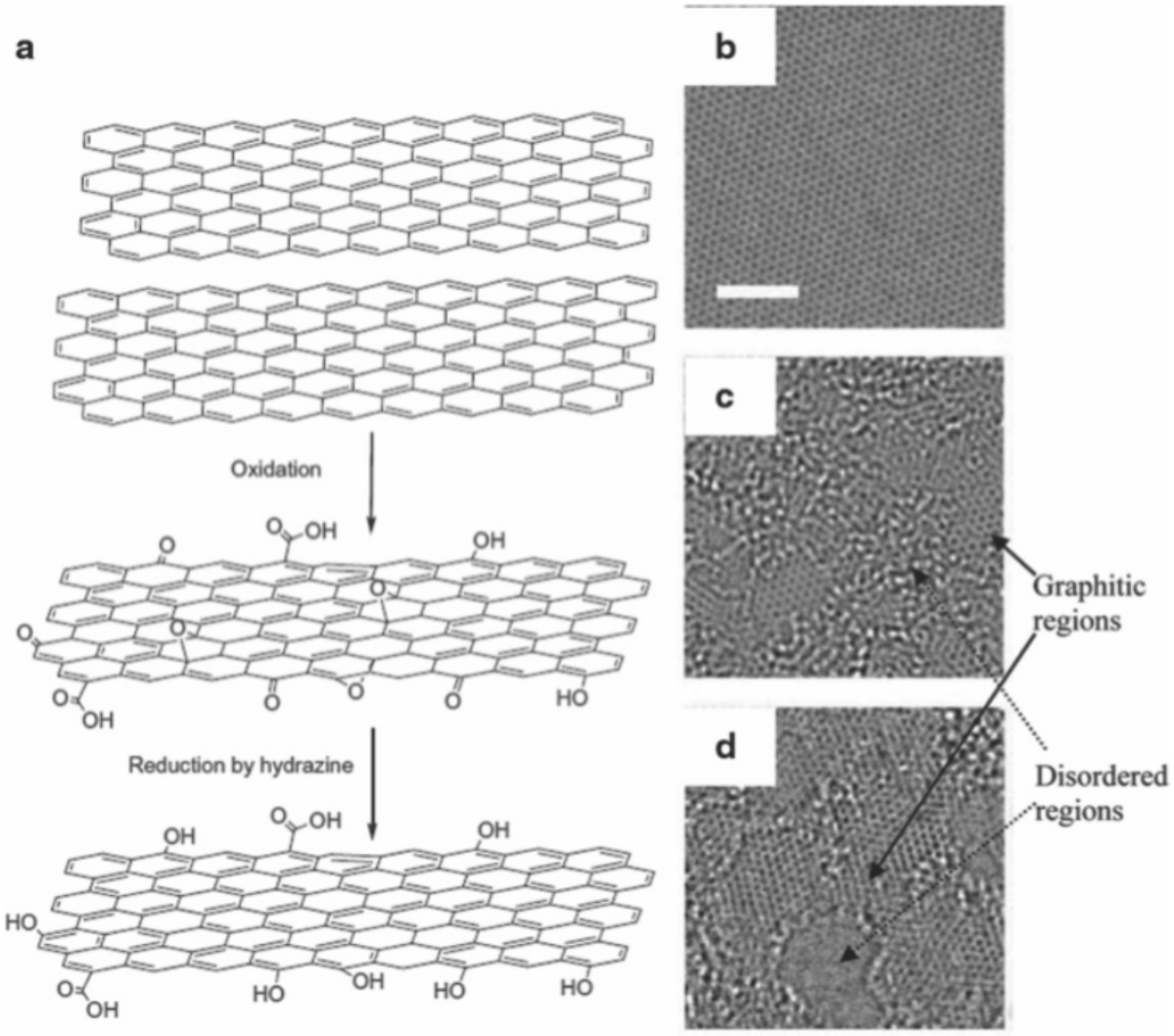


Figure 5. Reduction of graphene oxide (GO). (a) Oxidation of graphite to GO and reduction to reduced graphene oxide (rGO)[7]. (b) Single suspended sheet of graphene. (c) Single suspended sheet of GO. (d) Suspended monolayer of rGO.

#### 1.2.6.3 Synthesis of 3D graphene

Currently, various carbon materials are widely used as electrode materials for energy storage and conversion devices owing to their several advantages such as high conductivity, chemical stability for resistance to acid and alkaline, large active surface area. Since the first discovery of graphene nanosheets by Novoselov and Geim[3], numerous researchers have been fascinated by the study of this newly discovered carbon material and its various applications. Owing to its unprecedented electrical conductivity (calculated to be over 15000 $cm^2 V^{-1} s^{-1}$), excellent thermal conductivity (between 1500 and 2500 $W m^{-1} K^{-1}$), large surface area (2630 $m^2 g^{-1}$, much larger than those of carbon black of about 900 $m^2 g^{-1}$), high mechanical strength, and low density, 2D graphene has been widely used in many fields such as biomedical applications and energy applications (fuel cells, secondary batteries, and capacitors). Although 2D graphene has displayed excellent performance in many applications, two critical issues should be addressed. First, graphene sheets are easily restacked, which would block the active sites of electro-catalysts and increase the resistance to mass transfer, leading to poor electro-catalytic properties and second, graphene sheets lack pores ranging from micro- to macro-sized that favor rapid mass transfer, as well as increasing the surface area. Hence, 3D graphene-based structures with high porosity provide a way of tackling these two issues. Micro- (<2 nm) and meso-sized (2–50 nm) pores could significantly increase the active surface area, whereas macro-sized (>50 nm) pores act as open channels, which are crucial for accelerating the mass transfer rate and favoring accessibility to the surface. Despite the superior properties of 3D graphene such as a large active specific surface area, excellent electrical conductivity and outstanding mechanical strength, researchers have never stopped enhancing its efficiency via relentless study and investigation. However, the laborious mechanical exfoliation approach has prompted researchers to search for much more facile methods. In recent years, numerous methods of fabricating high-quality graphene have been developed in order to meet the requirements of large-scale production. 3D graphene first came into being in the form of an aerogel prepared by Vickery et al. via a freeze-drying method in 2009. Since then, various forms of 3D graphene macrostructures including aerogels, hydrogels, sponges, and foams have been formed by self-assembly, template-directed methods, etc. Here, aerogels and hydrogels of 3D graphene are basically classified by their preparation method, depending upon the method used for the extraction of liquid from the solid network of the gel system. The terms hydrogel is used when the liquid in the gel network is water and an organic solvent, respectively. When the liquid in the gel is extracted in the supercritical state of the liquid, these materials are called aerogels. The differences between a sponge and a foam mainly lie in their mechanical properties. A sponge can be compressed reversibly, whereas a foam is typically rigid and cannot be compressed repeatedly. For the synthesis approach, the self-assembly approach is the most widely used method, as it avoids the complex process of removal of the template used in the template-directed approach.

**1.2.6.2.1 Self-assembly-directed method**

The self-assembly method has been considered to be an effective strategy for the bottom-up construction of nano-scale materials. GO fabricated via the typical or modified Hummers method can act as a cost-effective building block for self-assembly into 2D graphene films or 3D macrostructures such as hydrogels,[31–33] aerogels,[33–38] papers,[39,40] sponges[39] and hybrid structures. This is because the planes and edges of GO sheets are decorated with an abundance of functional groups such as epoxy, hydroxyl, and carboxylic acid, which are hydrophilic, and the repulsive forces that are induced favor the stable formation of well-ordered macrostructures. The self-assembly behavior is mostly promoted by partial π–π stacking. In addition to GAs, graphene papers, graphene films, etc., are usually obtained via freeze-drying or $ScCO_2$ drying techniques instead of direct drying. This is because direct drying would cause the collapse of pores owing to the capillary forces induced by the evaporation of water. Freeze-drying could conserve most of the pores, because the water sublimates directly from the solid phase to the gas phase without destroying the skeleton. ScCO2 drying is another efficient way to eliminate surface tension during the water evaporation process to maintain pore volumes. Ruoff et al. obtained freestanding assembled GO paper employing a vacuum filtration and freeze-drying approach in 2007. Following this method, Liu et al. reported a technique for obtaining GO thin film and sponge using a speed vacuum concentrator and then drying processes. The key factor in forming GO sponges and films lies in the temperature-controlled evaporation rate. At 40 °C, the force derived from centrifugation is much larger than the force due to water evaporation. Thus, GO sheets tend to become connected into a network via the van der Waals force. However, at 80 °C, the evaporation force becomes the dominant force due to the increased evaporation rate, which results in the rapid generation of the first GO film layer at the liquid/vacuum interface, followed by the self-assembly of the second and third layers. RGO sponges and films were obtained via reducing the as-obtained GO by thermal annealing at 800 °C. In the same year, Shi et al. fabricated thermally stable 3D graphene hydrogels via a one-step hydrothermal reduction process in a sealed Teflon-lined autoclave at a relatively low temperature (i.e., 180 °C) for 12 h, which featured impressively high mechanical strength (the storage modulus was about 450–490 kPa) and high electrical conductivity (~$5 \times 10^{-3}$ S $cm^{-1}$). A hydrogel is a jelly-like network material that has a high-water content and an aerogel is a solid network material derived from a hydrogel, but the liquid is replaced by a gas. 3D GHs and GAs are usually formed in association with self-assembly procedures and have been extensively used in numerous applications. Fig. 2A shows the assumed mechanism of formation of a hydrogel, which indicates that the driving forces for the self-assembly of GSs are hydrophobic and π–π bond stacking interactions without any stirring disturbance, which means that a steric hindrance effect may benefit the conjugation of GSs. The outstanding mechanical properties of the self-assembled GHs fabricated by Shi's group are mainly a result of their strong building blocks,53 large sites of physical cross-linking via π–π stacking interactions and partial overlapping or coalescing of GSs, because they are different from GHs that are self-assembled via

conventional physical cross-linking owing to the weak interactions caused by hydrogen bonding, van der Waals forces, π–π interactions, and inclusion interactions. However, these methods should be modified or improved for the mass production of 3D graphene without the strict requirements for high temperature and pressure. In 2011, Chen et al. reported a more facile in situ self-assembly method under mild conditions for preparing a 3D architecture of GHs. They also studied the effect of various reducing agents including sodium hydrogen sulfite ($NaHSO_3$), sodium sulfide ($Na_2S$), vitamin C, hydrogen iodide, and hydroquinone on the reduction of GO. They found that the reducing time required to form the 3D structure varied using different reducing agents (Fig. 2C). The shape of the hydrogel can also be controlled by utilizing differently shaped reactors, revealing the isotropic shrinkage of self-assembled GO sheets. Besides, the 3D GH reduced by HI had the highest electrical conductivity (~110 S $m^{-1}$), which is most probably attributed to its higher density (~37 mg $cm^{-3}$ ) and higher level of reduction (the ratio of C/O is 8.5) compared with the use of other reducing agents. In addition to the direct self-assembly of GSs to form 3D graphene macrostructures, divalent ions (e.g., $Ca^{2+}$, $Ni^{2+}$, and $Co^{2+}$) and DNA molecules could also have the same effect. Jiang et al. reported the successful fabrication of a 3D graphene architecture driven by divalent ions at 120 °C and strengthened by polyvinyl alcohol (PVA). They showed the mechanism of divalent ion linkage, in which rGO sheets are interconnected by chemical and hydrogen bonds derived from water molecules, divalent ions and oxygen containing functional groups in the rGO sheets. Fig. 3B and C show as-obtained photos and SEM images of an rGO hydrogel obtained via divalent ion linkage. Fig. 3D shows the mechanism of controlled self-assembly of GO via DNA hybridization. Because divalent metal ions such as $Ca^{2+}$, $Co^{2+}$ and $Ni^{2+}$ and DNA molecules have superior biocompatibility, they could be employed in the fields of tissue engineering, bio-sensing or molecular storage. In order to cater to various applications, 3D graphene doped with B and N has been fabricated via a self-assembly approach. Wu et al. adopted ammonia boron trifluoride ($NH_3BF_3$) as both a reducing agent and a source of boron and nitrogen to prepare a B/N-co-doped 3D GA (BN-GA) used in all-solid-state supercapacitors (ASSSs). The nano and macroscale pores in the cross-linked GSs can be clearly seen in the SEM images of the BN-GA in Fig. 4. The calculated typical Brunauer–Emmett–Teller (BET) surface area reached 249 $m^2$ $g^{-1}$, as found by nitrogen adsorption–desorption analysis. An ASSS device assembled from a BN-GA displayed an increased specific capacitance (~65 F $g^{-1}$ ) and power density (~1600 W $kg^{-1}$ ) compared with non-doped devices. In 2012, the same group, Wu et al., decorated a N-doped 3D GA with $Fe_3O_4$ nanoparticles (NPs) for the ORR. The results showed the relatively more positive onset potential, higher current density and greater stability of the 3D N-doped GA compared with N-doped carbon black, both decorated with a uniform dispersion of $Fe_3O_4$ NPs, which revealed the significance of meso and macro pores in increasing the surface area of the graphene framework for applications in energy storage and conversion devices. Recently, Yu et al. have combined nano sized porous $NaTi_2(PO_4)_3$ particles with a 3D graphene network (GN) via a self-assembly method. This unique 3D structure could improve the electron/ion transfer rate

and ensure the integrity of the electrode structure, resulting in superior electrochemical performance when used in sodium batteries. With a similar method, the same group also reported the synthesis of Sn-based particles embedded in a 3D GN for lithium ion batteries. In general, 3D graphene obtained via a self-assembly method is also called 3D rGO, because it is reduced from GO. It is vital to control the level of reduction of GO via selecting an appropriate reducing agent, reaction temperature and pressure, because this is critical for balancing the hydrophilic properties and conductivity of the as-obtained 3D graphene.

**1.2.6.2.1 Template-directed methods**

In 2009, Ruoff et al. successfully fabricated a graphene film via a chemical vapor deposition (CVD) method utilizing copper foils (about 25 μm thick) as both surface substrate and catalyst at 1000 °C, with a mixture of methane and hydrogen as the carbon source. Then, GFs were first invented by Cheng et al., who chose nickel foam as the template, via a similar CVD method. The detailed procedure is illustrated in Fig. 6A. Specifically, carbon atoms were first obtained by the decomposition of $CH_4$ and diffused onto the Ni skeleton at 1000 °C, followed by the etching of Ni using hot $FeCl_3$ or HCl solution. Importantly, a layer of poly(methyl methacrylate) (PMMA) was needed for coating onto the surface of the graphene film before the etching step. Here, PMMA acted as a support to avoid the collapse of the graphene film during etching of the Ni skeleton. Finally, monolithic GFs were obtained after PMMA was dissolved in hot acetone. The as-prepared GFs suffered from thickness shrinkage of about 1.2 mm resulting from the liquid capillary force induced by the evaporation of acetone. The as-prepared GFs are flexible and display a superior electrical conductivity of about six times that of chemically derived graphene-based composites, which is mainly because their higher porosity of ~99.7% offers a rapid transport channel for charge carriers. Furthermore, the flexible GFs possess an ultralow density of about 5 mg $cm^{-3}$ and an ultra-large specific surface area of about 850 $m^2$ $g^{-1}$. These excellent properties of GFs have stimulated numerous researchers to fabricate GFbased electrode materials for promising applications in energy storage and conversion devices, sensors and electro-catalysts. Cu foam and Cu–Ni alloy foam have also been selected as templates other than Ni foam for synthesizing GFs. Ning et al. modified commercial Ni foam into porous Ni–Cu alloy foam with the pore sizes reduced from 200–500 μm to 5–100 μm. Thus, the specific surface area and conductivity of the GFs were increased remarkably. 3D graphene grown in situ based on Ni–Cu alloy foam exhibited remarkable discharge capacitance and stability when used as a supercapacitor electrode material. In addition to foam templates, colloidal spheres such as silica have also been employed to synthesize porous 3D graphene structures with a further reduction in the pore sizes to nanometers. Huang et al. assembled a hard template of silica spheres functionalized with methyl groups with GO sheets to generate porous 3D NGFs. The majority of the pore sizes were as small as 32.5 nm, which is similar to the size of the silica spheres. The specific surface area of the NGFs was about 851 $m^2$ $g^{-1}$. However, possibly owing to the aggregation of several

silica spheres, the larger-sized pores (~100 nm) contributed more to the main pore volume, from an analysis of the N2 adsorption–desorption plot (Fig. 7e). Wu et al. also adopted a method for the assembly of a 3D macroporous GA (MGA), using silica produced from tetraethoxysilane (TEOS) to generate mesopores of a size of about 2–3.5 nm in the 3D MGA framework. This hard-template-directed approach offers a facile route for generating mesopores in carbon-based materials to increase the specific surface area. Compared with the self-assembly-directed method, the template-directed synthesis of 3D GFs is a little more complex when removing the template and requires a high temperature. However, it provides a greater choice of carbon sources in addition to GO.

## 1.2 SERS

### 1.2.1 Introduction

Surface-enhanced Raman spectroscopy (SERS) was discovered in 1974 by three scientists (Fleischmann, Hendra, and McQuillan) at Southampton University. In their initial experiments, they discovered that the Raman spectrum of pyridine on a silver electrode showed an unusually strong Raman intensity [108]. Experimental investigation from multiple research groups showed that there are two underling mechanisms behind this Raman enhancement (chemical and the electromagnetic enhancement). Both mechanisms produce enhancement by causing a net change in the induced dipole moment. As stated previously in this chapter, the strength of the induced dipole moment for a Raman active molecule is given by , where is the molecular polarizabity and is the electric field strength. The first enhancement mechanism is electromagnetic enhancement and results from a change in the electric field strength . Electromagnetic enhancement is the dominant effect and occurs due to the enhancement of the electromagnetic field near the molecule of interest. This electromagnetic enhancement is caused by the interaction between the electromagnetic field and a nearby metallic substrate. The second form of enhancement is referred to as chemical enhancement and is a result of a change in polarizability induced by charge transfer and bond formation between the metallic substrate and the molecule of interest.

### 1.2.2 Fundamental Aspects

To understand these two mechanisms of SERS, it is important to first discuss the interaction of light with metallic surfaces. As incident light hits a metal surface, free electrons in the conduction band begin to oscillate. As the electrons oscillate the bulk electron charge is redistributed across the surface, and an electronic dipole is produced in the metallic lattice. This surface electron oscillation has discrete energy levels referred to as plasmons. When the incident light frequency matches the plasmon

oscillation frequency, a resonance state is achieved, referred to as surface plasmon resonance (SPR). At this resonance state, the magnitude of the surface plasmons is maximized and incoming light intensity is amplified and remitted. When the dimensions of the metallic structure are less than the wavelength of incident light, the SPR is highly dependent on the geometry, size, proximity, and composition of the nanostructures. When plasmon excitation occurs at the nanoscale, the electron density of the entire structure will oscillate. This overall surface electron oscillation is referred to as localized surface plasmon resonance (LSPR). LSPR results in an amplified electrical field near the particle surface and increased light scattering and absorption.

### 1.2.3 Chemical contributions

Current models explaining the experimentally observed signal enhancements in SERS are based on two contributions: the electromagnetic (EM) and the "chemical" enhancement (CE). The EM mechanism describes the enhanced local electromagnetic fields due to resonant excitation of plasma oscillations (plasmons) in the metallic nanostructure. This physical effect is by far the most dominant contribution, with standard SERS EFs in the wide range of $10^3$–$10^{10}$. Actually, the local field enhancements arising from the excitation of LSPRs do not require the presence of molecules at all; the latter are only necessary for the "frequency conversion" by means of Raman/inelastic light scattering. A direct interaction between the molecule and the underlying metal surface, however, is not covered at all by this effect. In contrast, the CE mechanism is related to the electronic properties of the adsorbate and acts by means of the increase in the electronic polarizability of the adsorbed molecule on the induced dipole $m_{ind}$ ; CE enhancements, of the order of one to three orders of magnitude, are significantly smaller than the EM contribution. First, charge transfer (CT) between the molecule in its electronic ground state and the metal can change the polarizability of the molecule, resulting in a change of the Raman scattering cross-section of the molecule. The same effect occurs in coordination chemistry when ligand molecules are bound to a metal center. Second, the energy levels of the adsorbate molecule usually differ from those of the molecule in its unbound or "free" state. For instance, let us assume that the laser excitation wavelength does not coincide with an electronic absorption band of the "free" molecule, but does coincide with one of the adsorbed molecule. The resonant excitation of electronic transitions in molecules is known as resonance Raman (RR) scattering. At the same time, new electronic excitation channels can arise through a photo induced CT mechanism, for example through CT from the metal to the adsorbed molecule. This is an integral component of the so-called CT resonance model, in which the transition energies depend on the energy separation between molecular and metallic energy levels. Electronic structure calculations on molecules at metal surfaces/clusters are therefore an extremely valuable approach for investigating the role of the above-mentioned contributions separately under controlled and a priori well- defined conditions. The interfacial structure of a molecule metal cluster and its optical properties can be modeled at the atomic scale by electronic structure calculations. Various

parameters can be investigated, including the bonding situation between the molecule and the metal nanostructure, the effect of surface roughness at the atomic scale, the effects of molecular and charge-transfer resonances, the effects of the incident laser wavelength, and the wavelength of Stokes Raman scattering ; in other words : electronic structure modeling can be used to disentangle the role of the individual contributions under the controlled and well-defined conditions[49-50] of a computer.

### 1.3 Superhydrophobic

#### 1.3.1 Fundamentals of superhydrophobic surface

Superhydrophobic surfaces are solid surfaces that are extremely difficult to wet; the contact angle (CA) of a water droplet on such a surface is larger than 150°, and roll-off angle/contact angle hysteresis is less than 10°. For an absolutely flat surface, wettability is determined by the surface free energy of the solid, which can be described by Young's equation[51] (Fig. 1a).

$$cos\theta_{\gamma} = \frac{\gamma_{sv}-\gamma_{sl}}{\gamma_{lv}} \qquad \text{eq 6}$$

where $\gamma_{sv}$, $\gamma_{sl}$ and $\gamma_{1v}$ are the surface free energies of solid–gas, solid–liquid and liquid–gas interfaces involved in the system, respectively. According to this equation, a solid material with a low surface energy is necessary to achieve a high CA. But this is not the only factor. For a real surface that is usually rough, topological roughness plays a crucial role in the wetting behavior of solid surfaces. To explain the relationship between surface roughness and wettability, two classical empirical models, the Wenzel regime and the Cassie–Baxter regime, have been extracted from various experimental data. In Wenzel's model, it is assumed that liquid completely fills the grooves of the rough surface. In contrast, for Cassie's case, the liquid is assumed to sit on top of the surface protrusions with air pockets trapped below. Therefore, a high CA may be achieved by increasing the surface roughness or introducing more buried air bubbles. The above theories have been successfully adopted to explain the underlying mechanism of the famous "lotus effect". It has been found that both the hierarchical micro-nanostructures (randomly distributed micro papillae and fine branch-like nanostructures) and the epicuticle wax materials (low surface energy coating) are responsible for the self-cleaning property, in agreement with the above theories

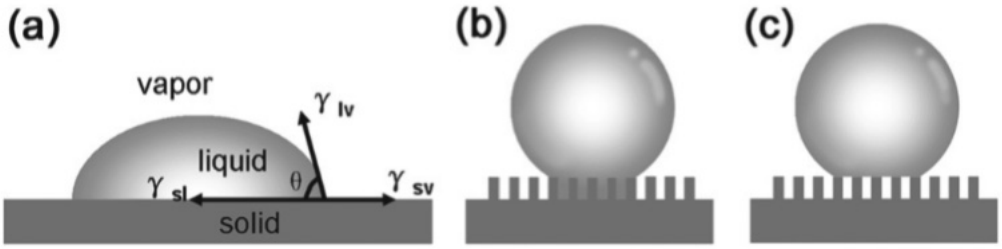


**Figure 6 : Schematic illustration of the wetting behavior of a water droplet on different solid substrates.(a) Young's model, (b) Wenzel's model, (c) Cassie's model[51].**

### 1.3.2 Superhydrophobic surface of graphene and graphene oxide

Surface wettability of graphene sheets plays a vital role in determining their compatibility with the desired environment. So, a deep understanding of the wettability of graphene and its related materials is fundamentally important for the development of graphene-based devices. Recently, several experimental and simulation studies have been focused on the surface properties and wettability of graphene films. Based on density functional theory, Leenaerts et al. indicated that graphene is strongly hydrophobic. They concluded that the binding energies between water molecules are larger than the associated adsorption energies on the graphene surface, such that water molecules form clusters on the graphene sheet. Quantum molecular dynamics simulations afford fundamental insight into the wetting behavior of water nanodroplets on a free-standing single-layer graphene sheet, and also allow incorporation of the polarization interaction, main-body effect and hydrogen-bond interactions into the prediction of wettability. The simulation results show that the graphene sheet has a CA of 87°[53]. Compared with the theoretical results, graphene grown by CVD gives a CA of 89.4°[54]. Besides, Shin et al.[55] reported that epitaxial graphene has a static contact angle (CA) of 92° and is slightly hydrophobic regardless of its thickness, close to that of highly ordered pyrolytic graphite (91°), while graphene reduced by hydrazine has a CA of 127° and a small interfacial energy with water. Proved both theoretically and experimentally, graphene has a natural hydrophobicity, which is essential knowledge for understanding the wetting behavior of water on the surface of such a material. In addition to pristine graphene, another important graphene related material that has been widely used for the fabrication of graphene-based devices is GO. GO is prepared by chemical exfoliation of natural graphite, and could be considered as a derivative of graphene with oxygen functional groups on its basal planes and edges. Due to the presence of OCGs, GO could be well dispersed in polar solvents such as water. Its ease of synthesis and solution processing capability make GO a promising precursor for the preparation of super- hydrophobic graphene surfaces. The wettability of the GO film is influenced by the OCG content on the surface. With various levels of oxidization, GO films exhibit different wetting properties. For instance, a GO film has a CA 67.4° compared to that of 30.7. Invariably, GO shows hydrophilicity owing to the chemical nature of the groups, such as carboxyl, hydroxyl and epoxy. To further increase its hydrophobicity, proper reduction treatments would be implemented. Drastic or partial removal of the hydrophilic OCGs would lower its surface energy, giving rise to much higher water CAs of the reduced GO (rGO).

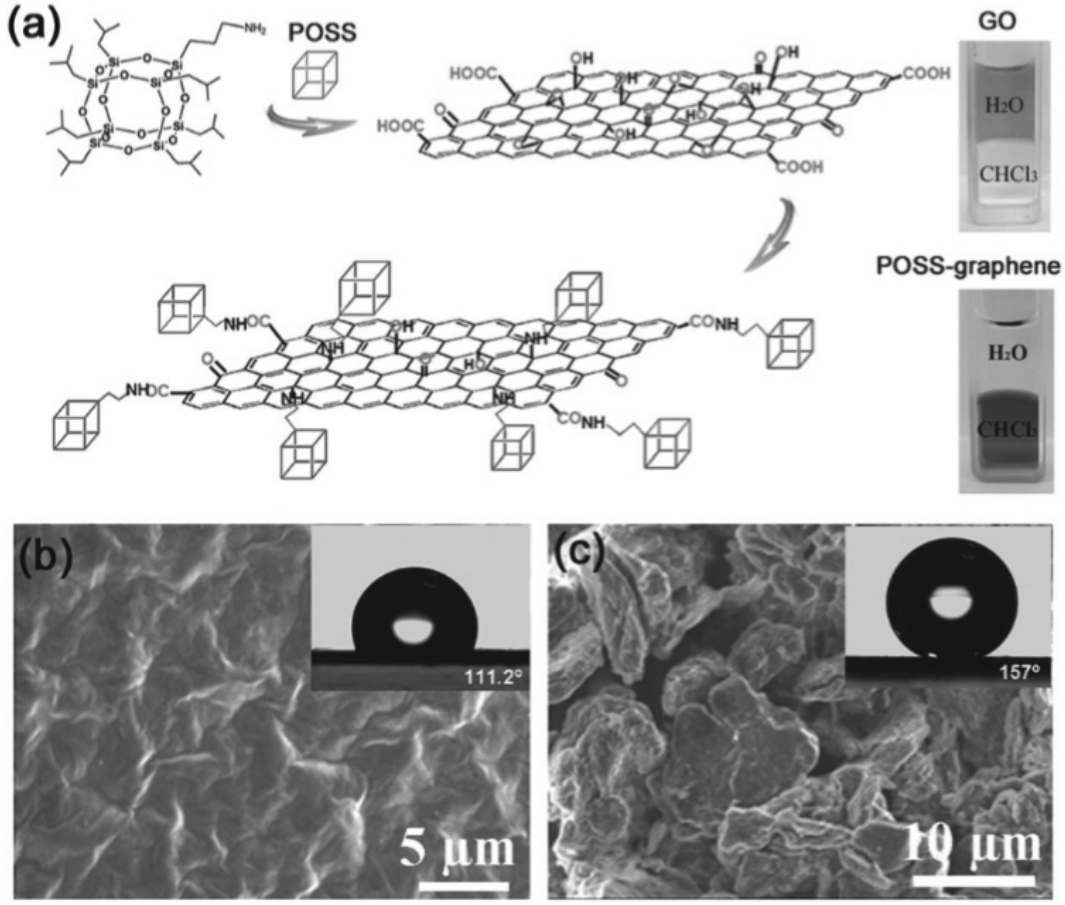


**Figure 7. (a) Surface modification of GP with POSS, photographs of the original GO in water and the synthesized POSS_graphene in $CHCl_3$. (b) SEM image of the POSS-grafted GO film, the inset shows a water droplet with CA ~ 111.2°. (c) SEM image of rough POSS-graphene film prepared from POSS-graphene with a corresponding water CA of 157°[54].**

### 1.4 Reference

1. KROTO, H. W.; HEATH, J. R.; S.C.O'BIEN; SMALLEY, R. F. C. R. E. C60:Buckminsterfullerene. *Nature* 1985, 318, 162-163.

2. IIJIMA, S. Helical microbutules of graphitic carbon. *nature* 1991, 354, 56-58.

3. Novoselov, K. S.; Geim, A. K.; Morozov, S. V.; Jiang, D.; Zhang, Y.; Dubonos, S. V.; Grigorieva, I. V.; Frirsov, A. A. Electric Field Effect in Atomically Thin Carbon films. *Science* 2004, 306, 666-669.

4. Soldano, C.; Mahmood, A.; Dujardin, E. Production, properties and potential of graphene. *Carbon* 2010, 48, 2127-2150.

5. Meitl, M. A.; Zhu, Z.-T.; Kumar, V.; Lee, K. J.; Feng, X.; Huang, Y. Y.; Adesida, I.; Nuzzo, R. G.; Rogers, J. A. Transfer printing by kinetic control of adhesion to an elastomeric stamp. *Nature Materials* 2005, 5, 33-38.

6. Chang, H.; Wu, H. Graphene-Based Nanomaterials: Synthesis, Properties, and Optical and Optoelectronic Applications. *Advanced Functional Materials* 2013, 23, 1984-1997.

7. Geim, A. K. Graphene : Staus and prospects. *Science* 2009, 324, 1530-1534.

8. Du, X.; Skachko, I.; Barker, A.; Andrei, E. Y. Approaching ballistic transport in suspended graphene. *Nat Nanotechnol* 2008, 3, 491-5.

9. Eda, G.; Chhowalla, M. Chemically derived graphene oxide: towards large-area thin-film electronics and optoelectronics. *Adv Mater* 2010, 22, 2392-415.

10. Kosynkin, D. V.; Higginbotham, A. L.; Sinitskii, A.; Lomeda, J. R.; Dimiev, A.; Price, B. K.; Tour, J. M. Longitudinal unzipping of carbon nanotubes to form graphene nanoribbons. *Nature* 2009, 458, 872-6.

11. Bai, J.; Zhong, X.; Jiang, S.; Huang, Y.; Duan, X. Graphene nanomesh. *Nat Nanotechnol* 2010, 5, 190-4.

12. Zheng, Q.; Li, Z.; Yang, J. Effects of N doping and NH2grafting on the mechanical and wrinkling properties of graphene sheets. *RSC Adv.* 2013, 3, 923-929.

13. Zheng, Q.; Geng, Y.; Wang, S.; Li, Z.; Kim, J.-K. Effects of functional groups on the mechanical and wrinkling properties of graphene sheets. *Carbon* 2010, 48, 4315-4322.

14. Shen, X.; Lin, X.; Yousefi, N.; Jia, J.; Kim, J.-K. Wrinkling in graphene sheets and graphene oxide papers. *Carbon* 2014, 66, 84-92.

15. Liu, F.; Ming, P.; Li, J. Ab initiocalculation of ideal strength and phonon instability of graphene under tension. *Physical Review B* 2007, 76.

16. Zakharchenko, K. V.; Katsnelson, M. I.; Fasolino, A. Finite temperature lattice properties of graphene beyond the quasiharmonic approximation. *Phys Rev Lett* 2009, 102, 046808.

17. Nizam Uddin, M.; Huang, Z.-D.; Mai, Y.-W.; Kim, J.-K. Tensile and tearing fracture properties of graphene oxide papers intercalated with carbon nanotubes. *Carbon* 2014, 77, 481-491.

18. Peres, N. M. R.; Guinea, F.; Castro Neto, A. H. Electronic properties of disordered two-dimensional carbon. *Physical Review B* 2006, 73.

19. Cadelano, E.; Palla, P. L.; Giordano, S.; Colombo, L. Nonlinear Elasticity of Monolayer Graphene. *Phys Rev Lett* 2009, 102, 235502.

20. kim, J.; Cote, L. J.; Kim, F.; Huang, J. Visualizing Graphene Based Sheets by Fluorescence Quenching Microscpoy. *J Am Chem Soc* 2010, 132, 260-267.

21. Nair, R. R.; Blake, P.; Grigorenko, A. N.; Novoselov, K. S.; Booth, T. J.; Stauber, T.; Preres, N. M. R.; Geim, A. K. Fine structure constant defines visual transparency of graphene. *Science* 2008, 320, 1308-1308.

22. Bae, S.; Kim, H.; Lee, Y.; Xu, X.; Park, J. S.; Zheng, Y.; Balakrishnan, J.; Lei, T.; Kim, H. R.; Song, Y. I.; Kim, Y. J.; Kim, K. S.; Ozyilmaz, B.; Ahn, J. H.; Hong, B. H.; Iijima, S. Roll-to-roll production of 30-inch graphene films for transparent electrodes. *Nat Nanotechnol* 2010, 5, 574-8.

23. Ni, Z. H.; Wang, H.; Kasim, J.; Fan, H. M.; Yu, T.; Wu, Y. H.; Feng, Y. P.; Shen, Z. X. Graphene Thickness Determination Using Reflection and Contrast spectroscopy. *Nano Lett* 2007, 7, 2758-2763.

24. Vlassiouk, I.; Smirnov, S.; Ivanov, I.; Fulvio, P. F.; Dai, S.; Meyer, H.; Chi, M.; Hensley, D.; Datskos, P.; Lavrik, N. V. Electrical and thermal conductivity of low temperature CVD graphene: the effect of disorder. *Nanotechnology* 2011, 22, 275716.

25. Yu, C.; Shi, L.; Yao, Z.; Li, D.; Majumdar, A. Thermal conductance and Thermopower of an individual single wall carbon nanotube. *Nano Lett* 2005, 5, 1842-1846.

26. Nika, D. L.; Balandin, A. A. Two-dimensional phonon transport in graphene. *J Phys Condens Matter* 2012, 24, 233203.

27. Berber, S.; Kwon, Y.-K.; Tomanek, D. Unusually High Thermal Conductivity of Carbon Nanotubes. *Phys Rev Lett* 2000, 84, 4613-4616.

28. Zhang, Y.; Small, J. P.; Pontius, W. V.; Kim, P. Fabrication and Electric Field Dependent transport Measurements of Mesoscopic Graphite Devices. *Applied Physics Letters* 2005, 86, 073104.

29. Novoselov, K. S.; Jiang, D.; Schedin, F.; Booth, T. J.; Khotkevich, V. V.; Morozov, S. V.; Geim, A. K. Two-dimensional atomic crystals. *proc natl acad Sci* 2005, 102, 10451-10453.

30. P.Blake, E. W. H.; Neto, A. H. C.; Novoselov, K. S.; Jiang, D.; R. Yang; T. J. Booth; Geim, A. K. MAking graphene visible. *Applied Physics ...* 2007, 91, 063124.

31. Jung, I.; Pelton, M.; Piner, R.; Dikin, D. A.; Stankovich, S.; Watcharotone, S. Simple Approach for high contrast optical imaging and characterization of graphene based sheets. *Nano Lett* 2007, 7, 3569-3575.

32. Chen, J. H.; Jang, C.; Xiao, S.; Ishigami, M.; Fuhrer, M. S. Intrinsic and extrinsic performance limits of graphene devices on SiO2. *Nat Nanotechnol* 2008, 3, 206-9.

33. Allen, M. J.; Tung, V. C.; B, K. R. Honeycomb Carbon : A Review of Graphene. *Chemical reviews* 2010, 110, 132-145.

34. Chen, Z.; Ren, W.; Gao, L.; Liu, B.; Pei, S.; Cheng, H. M. Three-dimensional flexible and conductive interconnected graphene networks grown by chemical vapour deposition. *Nat Mater* 2011, 10, 424-8.

35. De Arco, L. G.; Yi, Z.; Kumar, A.; Chongwu, Z. Synthesis, Transfer, and Devices of Single- and Few-Layer Graphene by Chemical Vapor Deposition. *IEEE Transactions on Nanotechnology* 2009, 8, 135-138.

36. Reina, A.; Thiele, S.; Jia, X.; Bhaviripudi, S.; Dresselhaus, M. S.; Schaefer, J. A.; Kong, J. Growth of large-area single- and Bi-layer graphene by controlled carbon precipitation on polycrystalline Ni surfaces. *Nano Research* 2010, 2, 509-516.

37. Zhang, Y. Review of Chemical Vapor Deposition of Graphene and Related Applications. *Acc. Chem Res* 2013, 46, 2329-2339.

38. Wissler, M. Graphite and carbon powders for electrochemical applications. *Journal of Power Sources* 2006, 156, 142-150.

39. Sasa, T.; Takahashi, Y.; Mukaibo, T. Crystal structure of graphite bromine lamellar compounds. *Carbon* 1971, 9, 407-416.

40. Shih, C. J.; Vijayaraghavan, A.; Krishnan, R.; Sharma, R.; Han, J. H.; Ham, M. H.; Jin, Z.; Lin, S.; Paulus, G. L.; Reuel, N. F.; Wang, Q. H.; Blankschtein, D.; Strano, M. S. Bi- and trilayer graphene solutions. *Nat Nanotechnol* 2011, 6, 439-45.

41. Eda, G.; Chhowalla, M. Graphene based composite thin films for electronics. *Nano Lett* 2009, 9, 814-818.

42. Stankovich, S.; Piner, R. D.; Nguyen, S. T.; Ruoff, R. S. Synthesis and exfoliation of isocyanate-treated graphene oxide nanoplatelets. *Carbon* 2006, 44, 3342-3347.

43. Stankovich, S.; Dikin, D. A.; Dommett, G. H.; Kohlhaas, K. M.; Zimney, E. J.; Stach, E. A.; Piner, R. D.; Nguyen, S. T.; Ruoff, R. S. Graphene-based composite materials. *Nature* 2006, 442, 282-6.

44. Wei, L.; Jiang, W.; Yuan, Y.; Goh, K.; Yu, D.; Wang, L.; Chen, Y. Synthesis of free-standing carbon nanohybrid by directly growing carbon nanotubes on air-sprayed graphene oxide paper and its application in supercapacitor. *Journal of Solid State Chemistry* 2015, 224, 45-51.

45. Vickery, J. L.; Patil, A. J.; Mann, S. Fabrication of Graphene-Polymer Nanocomposites With Higher-Order Three-Dimensional Architectures. *Advanced Materials* 2009, 21, 2180-2184.

46. Xu, Y.; Sheng, K.; Li, C.; Shi, G. Self-assembled Graphene Hydrogel via a one-step hydrothermal process. *ACS nano* 2010, 4, 4324-4330.

47. Zhou, Y.; Yen, C. H.; Fu, S.; Yang, G.; Zhu, C.; Du, D.; Wo, P. C.; Cheng, X.; Yang, J.; Wai, C. M.; Lin, Y. One-pot synthesis of B-doped three-dimensional reduced graphene oxide via supercritical fluid for oxygen reduction reaction. *Green Chem.* 2015, 17, 3552-3560.

48. Fleischmann, M.; Hendra, P. J.; McQuillan, A. J. Raman spectra of pyridine adsorbed at a silver electrode. *Chemical Phyics Letters* 1974, 26, 163-166.

49. Zhao; Jensen, L.; Schatz, G. C. Pyridine-Ag 20 Cluster : A model System for studting surface-enhaced Raman scattering. *J Am Chem Soc* 2006, 128, 2911.

50. Smith, W. E. Practical understanding and use of surface enhanced Raman scattering/surface enhanced resonance Raman scattering in chemical and biological analysis. *Chem Soc Rev* 2008, 37, 955-64.

51. Young, T. An Essay on the Cohesion of Fluids. *PHILOSOPHICAL TRANSACTIONS* 1805, 95, 65-87.

52. WENZEL, R. N. RESISTANCE of SOLID SURFACES TO WETTING BY WATER. *INDUSTRIAL AND ENGINEERING CHEMISTRY* 1936, 28, 8.

53. LI, H.; Zeng, X. C. Wetting and Interfacial Properties of Water Nanodroplets in Contact with Graphene and MOnolater Boron-Nitride Sheets. *ACS nano* 2012, 6, 2401-2409.

54. Dong, X.; Chen, J.; Ma, Y.; Wang, J.; Chan-Park, M. B.; Liu, X.; Wang, L.; Huang, W.; Chen, P. Superhydrophobic and superoleophilic hybrid foam of graphene and carbon nanotube for selective removal of oils or organic solvents from the surface of water. *Chem Commun (Camb)* 2012, 48, 10660-2.

55. Lin, Z.; Liu, Y.; Wong, C. P. Facile fabrication of superhydrophobic octadecylamine-functionalized graphite oxide film. *Langmuir* 2010, 26, 16110-4.

# CHAPTER 2 : THREE-DIMENSIONAL GRAPHENE NANO-NETWORKS WITH HIGH QUALITY AND MASS PRODUCTION CAPABILITY VIA PRECURSOR-ASSISTED CVD

## 2.1 Introduction

Three-dimensional (3D) bi-continuous structures with controlled symmetry and periodicity have found use in many applications in photonic crystals, phononic crystals and MEMS.[1, 2] In addition, the large surface area and the availability of 3-dimensional responses to external stimuli provide further potential for using 3D structures in diverse areas of energy-related materials and tissue engineering.[3, 4]

Graphene is a one-atom-thick planar sheet that is densely packed with $sp^2$-bonded carbon atoms in a honeycomb crystal lattice with high optical transmittance, excellent electrical conductivity, high flexibility and mechanical stability, large theoretical specific surface area, and unique transport properties.[5-8] Graphene grown on metal film by CVD via carbon dissolution and a segregation mechanism on a metal catalyst surface has superior conductivity because it has fewer defects and a relatively large domain size.[9-14] Potential problems in CVD growth on a metal film are that the formation of single-crystalline graphene is limited to the 2D plane and production is limited to small quantities. The availability of more sophisticated 3D graphene nanonetworks (3D-GN) on a bulk scale would enable important advances in energy-related materials, heat sinks, and cell culture plates by taking advantage of large surface areas, outstanding high electrical/thermal conductivity, and three dimensional environments. For example, it has recently been reported that 3D graphene networks grown on a 3D nickel frame have excellent mechanical strength, supercapacitance, and thermal transport properties due to the nature of the 3D structures.[6, 15, 16] However, the dimensions of the structures fabricated by this approach are confined by the dimensions of the available nickel frame and are restricted to a scale of a few hundred micrometers, which might in turn hamper a variety of potential applications for the 3D graphene. Alternatively, a 3D graphene-frame on a micron scale has been fabricated by vacuum filtration of chemically modified graphene, although performance was rather low due to the use of reduced graphene oxide.[17, 18] Exploring ways to synthesize graphene that allow for dimensional tunability down to the nanometer scale without loss of its original characteristics could play an important role in both fundamental study and the realization of future graphene applications. So far copper and nickel have been commonly used as metal catalysts for CVD growth of graphene with well-established methods, and minor progress has been recently achieved in growing multilayer graphene film on iron-based catalysts, which have been widely used for growing carbon nanotubes.[19-21] Utilizing iron as a catalyst will also broaden the applicability of graphene and be an attractive avenue of research, since iron is the fourth most common element in the earth's crust and it is nontoxic, inexpensive, and easy to remove.

Supercapacitors are attractive as alternative energy storage devices to batteries and fuel cells due to

their fast charging and discharging rates at high power densities, long life cycle, simple principle, and low maintenance cost.[22-25] Among two different classes of supercapacitors classified by their energy storage mechanism, electrochemical double-layer capacitors (EDLCs) and pseudocapacitors (PCs), EDLCs use the adsorption/desorption of ions forming an electrical double-layer at the interface between an electrode and an electrolyte for storing charge. It is critical to guarantee effective surface area and surface properties of the electrode. In addition to high specific surface area, several other parameters, such as good electric conductivity, appropriate pore size and distribution, and electrochemical, thermal, and mechanical stability, are equally important to supercapacitor performance. In light of these requirements, porous carbon materials have been suggested as promising materials for EDLCs.[26, 27] However, most porous carbon-based materials with high specific surface area suffer from rather low conductivity, which restricts their application in high performance supercapacitors. On the other hand, graphene provides an ideal alternative to existing EDLC materials, since it has very high electrical conductivity and excellent chemical and mechanical stability and extremely large surface area. However, its theoretical value of parameters such as conductivity ($10^{-6}$ Ω/□) and surface area (2630 $m^2$/g) still need to be realized, at least to some extent.[28, 29]

Here, for the first time, we report a bi-continuous 3D-GN grown via a substrate-free CVD technique using solution processed iron precursors, which potentially allow for any arbitrary shape of graphene with dimensional scalability and mass-production capability. Graphene is grown on a 3D assembly of colloidal silica infiltrated with a PVA/iron precursor solution. Annealing PVA/$FeCl_3$ in a hydrogen environment reduces the iron, which can serve as a catalyst for the dissolution of carbon during the subsequent graphene growth process. A 3D-GN has a substantially improved geometrical surface area of 1,025 $m^2$/g and a resistance of 52 S/cm, which greatly exceeds the values of traditional 3D graphene structures, e.g., graphite with 0.6 $m^2$/g and tens of kΩ/□, respectively.[30-33] Moreover, as a result of employing solution-prepared metal precursors, high-quality 3D graphene can be grown on any inert substrate, such as $Al_2O_3$, quartz or GaN, etc., enabling the production of ready-to-use graphene for use in the semiconductor industry. As a proof of concept, we have demonstrated that 3D-GN-based EDLC exhibits an excellent specific capacitance of 325 F/g and 90% retention after 1000 cycles. The superior performance of a 3D-GN as an electrode for supercapacitors is attributed to the realization of the effective synergies of the great conductivity and large surface area of graphene in the form of a 3-dimensional network with proper pore sizes. Artificially created 3D-GNs with controlled shape and spacing offer excellent potential for application in areas where the advantages of both graphene and nanoscale 3D structures are needed, such as 3D electrodes, energy conversion/storage devices, and thermal management systems.

**2.2 experimental methods**

**2.2.1 Preparation of CS/PVA-FeCl3•6H2O composite thin film**

Poly vinyl alcohol (PVA, Mw = 31,000-50,000) and $FeCl_3 \cdot 6H_2O$ were obtained from Aldrich Chemical Company and used without any further purification. PVA (10 wt%) was dissolved in DI-water at 90 $^oC$ and then mixed with percents of 100, 200, 350, and 600 phr (phr: part per hundred parts of resin) by weight of $FeCl_3 \cdot 6H_2O$. PVA/$FeCl_3$ composite thin films were prepared by self-assembly of CS, as reported elsewhere. Any impurities in the solution were filtered through a 0.2 m cellulose acetate syringe filter and the filtrated solution was spin-coated on a 300 nm $SiO_2$/Si substrate. The prepared composite thin films were dried in a vacuum oven for one day. 3D-GN was p-doped by dipping in 20 mol % of $HNO_3$ solution for 30 min followed by washing in D.I. water in order to enhance the conductivity for supercapacitance measurements.

**2.2.2 Fabrication of the 3D-GN**

The prepared composite films were placed in a quartz tube (Scientech Co.) with an outer diameter of 120 mm, heated to 1,000 $^oC$ in a $H_2$ (100 sccm)/Ar atmosphere at 4 torr with a heating rate of ~20 $^oC$/min, and then placed in isothermal conditions for 30 min. After annealing, the samples were cooled to an ambient temperature. The 3D-GN/Fe sample on a 300 nm $SiO_2$/Si substrate was then immersed on BOE consisting of HF (5%) and HCl (3%) for 48 hrs to remove the $SiO_2$ substrate and iron simultaneously.

**2.2.3 Characterization of 3D-GN**

The structures of the samples were characterized by SEM (Nova Nano-SEM 230, 10 kV), TEM (JEM-2100, 200 kV) and Raman spectroscopy (WITec, alpha300R, excited by a 532nm laser). X-ray diffraction measurements were carried out with a Rigaku Co. High Power X-Ray Diffractometer D/MAZX 2500V/PC from $20^o$ to $80^o$. Surface area determination was performed by Brunauer-Emmett-Teller (BET) methods using an ASAP 2000 surface area analyzer (Micrometerics Instrument Corp.). The conductivity of 3D-GNs (both film and powder type) were characterized by 4 point-probe (Dasol Eng, FPP-RS8, pin-spacing 1 mm, pin-radius 100 um). To measure conductivity of powder type 3D-GN, the pellet with a diameter of 13 mm and thickness of 50 m was prepared by mechanical milling and subsequent pressurizing (1000 kg/$cm^2$) of the 3D-GN. The resistances between film type and powder type did not show noticeable difference.

### 2.2.4 Electrochemical measurement

The electrochemical properties of supercapacitor electrodes were measured in three-electrode systems by cyclic voltammetry using a computer controlled electrochemical interface (Solartron SI 1287) from 0 to 1 V at room temperature. 3D-GNs, a platinum mesh, Ag/AgCl, and 1M $LiClO_4$ in ACN were used as the working electrode, counter electrode, reference electrode, and electrolyte, respectively. To examine the electrochemical properties, the 0.2 mg of electro-active material (3D-GN) was mixed with acetylene black (10%), and polyvinylidenedifluoride (PVDF, 10wt.%) as a binder, and then the mixture was pasted onto a Ni electrode (0.28 $cm^2$) and dried at 150 $^oC$ for 20 min in an air atmosphere. The cyclic voltammetry was carried out at different scan rates ranging from 5 mV/s to 100 mV/s. Electrochemical impedance spectroscopy (EIS) was carried out at a frequency range from 100 kHz to 0.1 Hz using a potentiostat (Versa STAT 3, AMETEK). The control sample for EIS measurement was fabricated with 95 % of ethylene carbon and 5 % of PVDF.

## 2.3 Results and discussion

Figure 8 shows the four steps of the fabrication process for the 3D-GN. First, surface-activated colloidal silica (d = 30 nm, 150 nm, and 220 nm) obtained by treatment with $H_2SO_4$ were self-assembled using Colvin's method[34] into near single crystalline opals with a face-centered cubic (FCC) structure on a 300 nm thick $SiO_2$/Si substrate with a thickness of 3 um. Then a solution of PVA-$FeCl_3$ was infiltrated into the 3D-assembly of silica colloids. We chose iron chloride hexahydrate ($FeCl_3 \cdot 6H_2O$) and water-soluble polyvinyl alcohol (PVA) as a precursor of the Fe catalyst and a solid carbon source for graphene growth, respectively. PVA was chosen because it can easily form a homogeneous dispersion with the iron precursor ($FeCl_3$, in this case) due to the electrostatic interaction between the hydroxyl groups of PVA and iron ions in the $FeCl_3$ solution.[35, 36] In the third step, the composite film of 3D PVA-$FeCl_3$/CS on the $SiO_2$/Si substrate was heated to 1,000 $^oC$ in a quartz tube. Annealing the 3D PVA-$FeCl_3$/CS composite in a hydrogen environment at high temperature reduced the iron ions (III) into iron (0) and subsequent growth of graphene using PVA as a carbon source on the surface of the iron metal. This process is supported by a recent report demonstrating CVD graphene growth on an iron film substrate.[21] In the final step, iron was removed with the HF/HCl solution leaving near single-layer 3D-GN structures on the $SiO_2$/Si substrate. Figure 9 shows the morphological characteristics of a representative 3D-GN obtained by CVD growth followed by removing the iron and the assembly of 220 nm silica particles. Figure 9a is a scanning electron microscope (SEM) image of a 3D assembly of PVA-$FeCl_3$/CS with a thickness of 3 um. Figure 9b is a SEM image of a low-density 3D-GN created from graphene growth

and subsequent removal of iron/CS. The optimum ratio of PVA to $FeCl_3$ was determined by careful control of the pressure and flow rate of the gas during the CVD process. The thickness of the 3D-GN generated from the removal of the CS template was reduced to approximately 80% of the original thickness due to the loss of carbon materials and a slight collapse of the 3D-GN near the substrate caused by the surface tension of aqueous solvent during the drying process. However, once the nanopore structures formed, they were rigid and stable enough to be used for further applications as expected from the high modulus (1,100 GPa) of graphene reported elsewhere.[6, 28] Figures 9c and 9d are a TEM image of the 3D-GN near the edges clearly showing a nano-cavity of the 3D-GN and a close-up image of a single unit cell of the 3D-GN with a diameter of 220 nm, respectively. Additionally, we occasionally observed another set of nanopores with diameters of ~ 40 nm on the surface of a single graphene ball. This is likely attributable to the removal of iron nano domains formed due to the agglomeration of iron during the annealing process. Figure 9e is a selected area diffraction image of a single unit cell of graphene, revealing the (nearly) single crystalline nature of graphene. Besides the formation of the network in the film, a bulk scale of the 3D-GN fabricated by the drop-casting of solution followed by CVD also yielded a comparable quality of graphene (Raman, resistance, etc.).

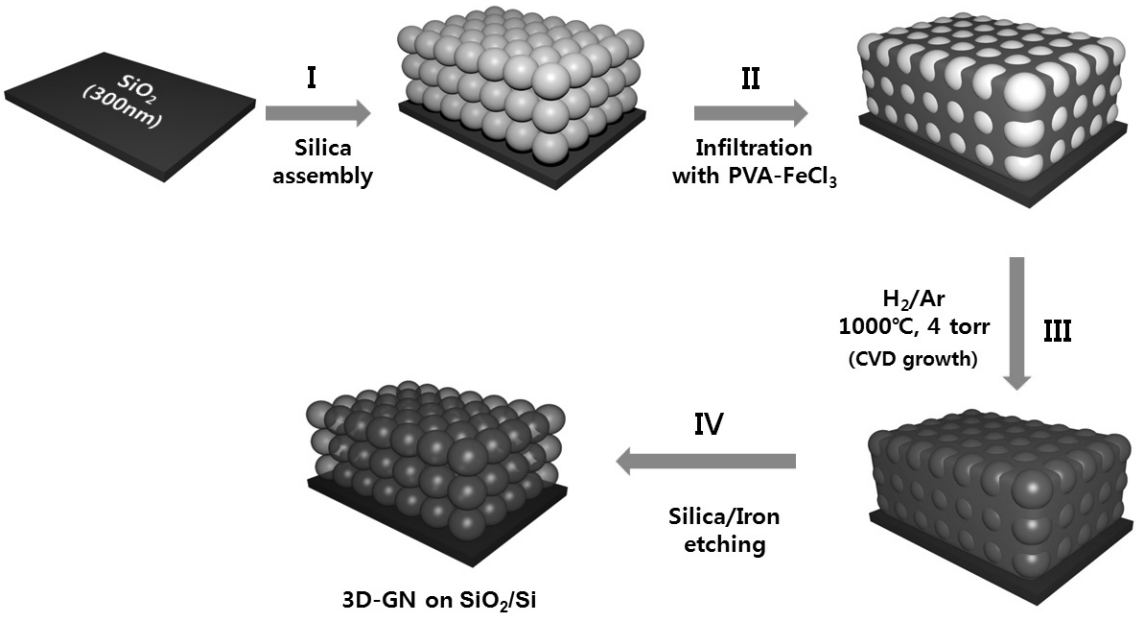


**Figure 8 : Schematic illustration of the fabrication process for a 3D-GN. I) Self-assembly of CS on $SiO_2$/Si substrate. II) Infiltration of PVA-$FeCl_3$ into 3D assembly of CS. III) Graphene growth by CVD on 3D PVA-$FeCl_3$/CS assembly. VI) Iron/CS etching, leaving the 3D-GN**

.

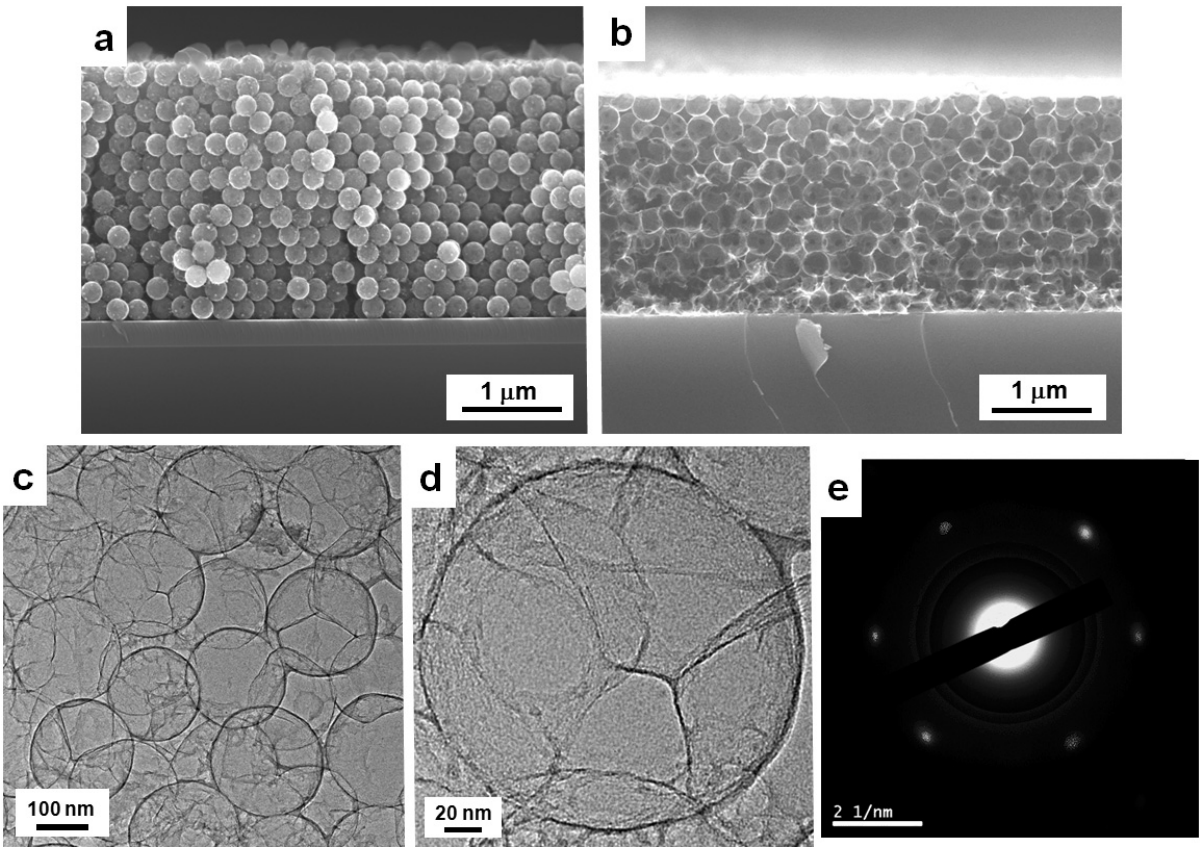


**Figure 9. Morphological characterizations of 3D-GN. (a) SEM image of 3D PVA-$FeCl_3$/CS (220 nm). (b) SEM image of 3D-GN created from graphene growth followed by removal of iron. (c) TEM image of 3D-GN taken near the edges. (d) Close-up image of a single graphene ball. (e) The selected area electron diffraction (SAED) pattern showing the single crystalline nature of the graphene ball in the image of (d).**

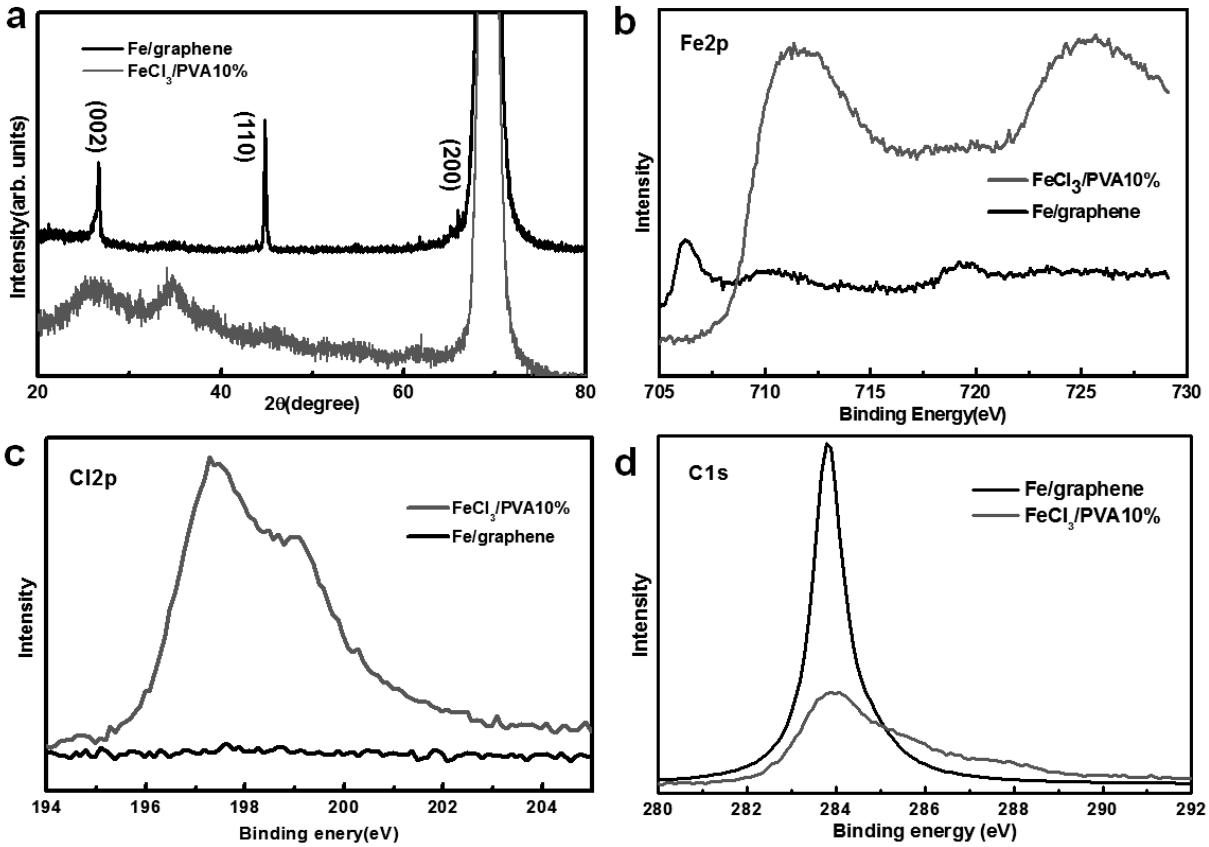


**Figure 10 : X-ray diffraction (XRD) and X-ray photoelectron (XPS) spectra before (all in red) and after (all in black) annealing of PVA-FeCl3/SC (220nm) film at a FeCl3 concentration of 350 phr. a) The XRD of pristine iron chloride hexahydrate (FeCl3•6H2O) is shown in red and that of an annealed film of PVA-FeCl3/CS composite (3D-GN containing iron) is in black. b-d) XPS spectra of Fe, Cl, and C in the film.**

X-ray diffraction (XRD) measurements were made to confirm the reduction of Fe (III) to Fe (0). Figure 10 (a) shows the XRD data of the PVA-$FeCl_3$/SC(220 nm) film at a $FeCl_3$ concentration of 350 phr before and immediately after annealing in a $H_2$ gas environment. Compared to the data taken from the pristine PVA-$FeCl_3$ film showing many broad and undefined peaks in red, two sharp peaks corresponding to the (200) and (110) planes of Fe (0) and another strong and sharp peak indexed to the (002) plane of graphene are evolved for the annealed sample in black (3D-GN containing iron)[37]. These peaks confirm that the iron ions are completely reduced to the nearly single crystalline iron metal with the preferred growth direction in the (110) plane, which shows the capability of successfully creating single crystalline graphene which appears at $2\theta = 26^{o}$.

The transformation of $FeCl_3$ to iron metal followed by graphene growth can be further confirmed by analyzing the X-ray photoelectron spectroscopy (XPS) spectra of iron, chlorine, and carbon in the same samples as the ones for XRD. Figures 10(b-d) show the XPS spectra of Fe2p, Cl2p, and C1s in pristine PVA/$FeCl_3$ (all in red) and converted 3D-GN/Fe (all in black) after the CVD growth procedure. Major differences between the iron ion species and metallic iron can be seen in the Fe2p region at around 700-730 eV, as shown Figure 10b. The Fe2p peak from the pristine PVA/$FeCl_3$ sample is deconvoluted into two major peaks, at 711.5 eV and 724.54 eV, corresponding to the binding energy of $Fe^{3+}$ in $FeCl_3$ and $Fe_2O_3$, respectively, which suggests the coexistence of $FeCl_3$ and oxidized $Fe_2O_3$.[38, 39] On the other hand, a peak at around 704 eV, corresponding to the binding energy of metal ions, appears for the annealed samples, clearly indicating the reduction of iron ions. The peak between binding energies of 195 eV and 204 eV in the XPS spectra (in Figure 10c) reveals the presence of chlorine in the samples. The two broad peaks in red at binding energies of 198.8 eV and 199.95 eV, corresponding to 2p3/2 and 2p1/2 electrons of chlorine ions ($Cl^{-}$), respectively, in the pristine sample and the disappearance of the chlorine ion peak in the 3D-GN/Fe sample suggest that the chlorine is completely evaporated under the high temperature growth conditions of the 3D-GN. Finally, compared to the broad and significantly low C1s peak in the pristine samples in Figure 3d, the intense, sharp peak in the 3D-GN/Fe, centered at 284.18 eV, which originated from the C-C or C=C bond, indicates the conversion of amorphous carbon into high quality graphene. A full width at half maximum (FWHM) of 0.82 was obtained for the 3D-GN; this is comparable to the FWHM of a high quality single layer of graphene.[40, 41]

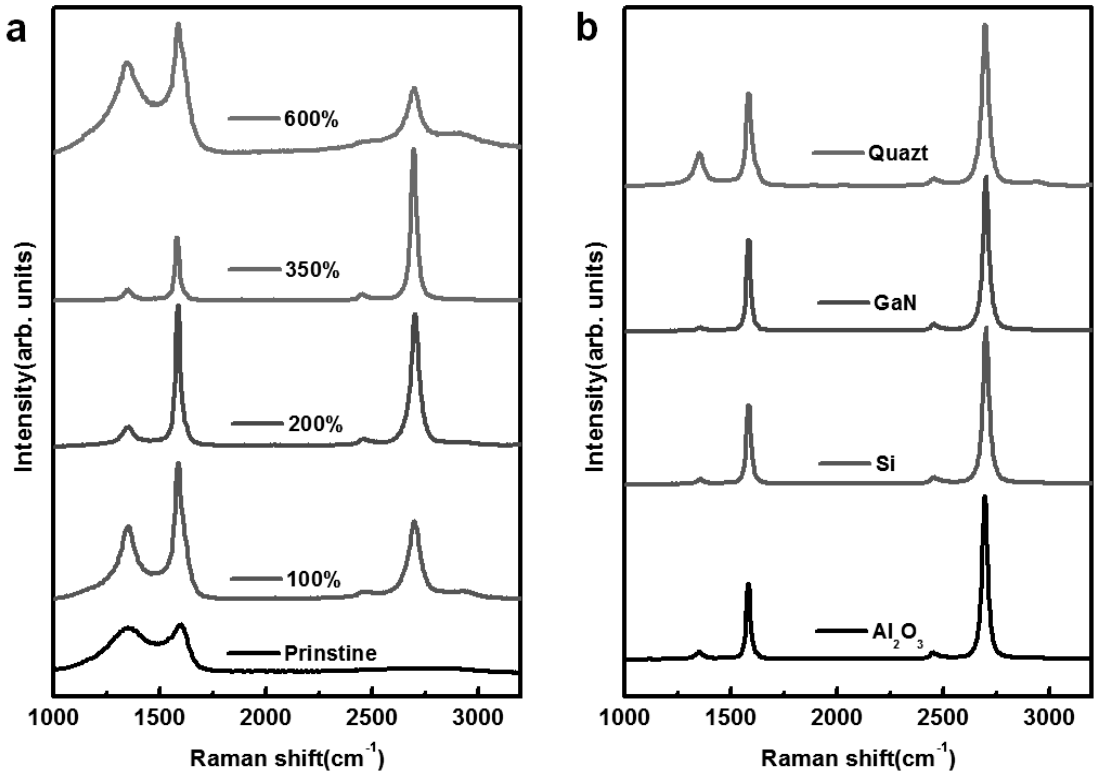


**Figure 11 : Raman spectra of 3D-GNs grown by CVD. a) Raman spectra with various composition ratios (phr: parts per hundred parts of resin) of PVA-FeCl3 by templaing 220 nm of SC. The Raman spectrum of pristine PVA after annealing at 1000 ºC in a H2 environment is presented in black. b) Raman spectra of 3D-GNs grown on various substrates by templating PVA-FeCl3 solution at a FeCl3 concentration of 350 phr 220 nm of SC. There is basically no restriction on the choice of substrate as long as it is stable and inert at high temperature.**

Figure 11 shows the Raman spectra of 3D-GNs synthesized by the diffusion and precipitation of carbon on the surface of 3D iron networks with various composition ratios of PVA to iron precursors. On the basis of previous reports that describe the growth of graphene on iron, one significant issue to be considered is that the relatively high solubility of carbon in iron could lead to the formation of multi-layer graphene with some defective areas.[21] We found that the initial amount of iron and carbon greatly affected the quality of graphene and the structural formation of the 3D-GN, since both elements are nearly used up during the growth process. Optimum growth conditions of graphene on PVA-$FeCl_3$/3D-CS were determined by careful control of the pressure and the flow rate of the gas at 1000 $^oC$ in all the experiments during CVD until we acquired the best Raman peak. The typical Raman spectrum of the 3D-GN at various iron to PVA ratios characterized at more than 20 random locations are compared with that of pristine $FeCl_3$/PVA with broad, strong D and G peaks as shown in the bottom of Figure 11(a). The creation of graphene in the 3D-GN can be verified by the decrease in the intensity of the D band and the evolution of sharp G and 2D bands at the higher frequency region. The intensity of the G band steadily increased as the amount of $FeCl_3$ increased (from bottom to top) implying the formation of a planar configuration of $sp^2$ bonds. The dramatic increase in intensity of the 2D band of the 3D-GN at 350 phr indicates high-quality of single-layer graphene. The negligible D peak around 1350 $cm^{-1}$ for the 350 phr sample suggests that the 3D-GN at 350 phr has few defects or symmetry-broken sites. The maximum ratio of $I_{2D}/I_G$ and the minimum ratio of $I_D/I_G$ optimized at 350 phr are 3.27 and 0.18, respectively. Therefore, the Raman spectra indicate that amorphous parts of carbonized-C are nearly used up and transformed into near single-layer 3D graphene networks when the ratio of PVA to iron was set at around 1:3.5. Surprisingly, the average sheet resistance of the 3D-GN obtained from more than 20 samples was 52 S/cm, which is close to the highest recorded value to date for a single layer of graphene. Moreover, the average sheet resistance of the 3D-GN before the removal of iron was ~50 Ω/□, implying potential for the direct use of 3D-GN/iron as a porous 3D electrode. More importantly, one of the significant advantages of the proposed method is that it allows for mass-production. Since the iron precursor can be homogenously dispersed with the carbon source to form the graphene frame, there is essentially no limit to the scale of production for this type of substrate-free CVD. For example, we could obtain 2 g of 3D-GN per batch of CVD, which is comparable to 2050 $m^2$ of planar 2D graphene based on the surface area of our 3D-GN. Due to such large scale production, BET measurement is readily available. The surface area of the 3D-GN obtained by templating 220 nm uniform silica particles (in Figure 10) was measured to be 448 $m^2/g$ and the pore size of a 3D-GN range from approximately 210-230 nm in diameter, with some much smaller mesopores with a mean diameter of 14 nm, as shown in Figure S8. The surface area of 448 $m^2/g$ is much greater than that of same size CS templates (13 $m^2/g$), which can be attributed to the presence of cavities as well as a few layers in graphene. We believe further improvement of the physical characteristics of 3D-GNs will be possible, i.e., much smaller pores by using a smaller size uniform silica template and better conductivity with more systematic control of

composition ratios as well as growth conditions. In fact, we were able to obtain a 3D-GN with a specific surface area of 1,025 $m^2/g$ and conductivity of 12 S/cm by templating silica particles with a dimension of 20-30 nm in diameter on a bulk scale. Even though they had lower uniformity in particle size and shape and somewhat aggregated morphology compared to the larger size particles, comparable quality of Raman peaks and other characteristics to those of the uniform larger size and well assembled 3D-GNs were observed, as shown in the Supporting Information. Another very useful benefit of this technique compared to previously reported methods is that the graphene growth does not restrict the choice of substrate due to the use of metal precursor solutions, which essentially permits the dimensional scalability. Furthermore, this circumvents the need for a transfer process which can lead to the introduction of additional defects. Figures 12(b) shows the Raman spectra of a 3D-GN grown on any arbitrary substrate such as bare silicon, sapphire, GaN, or quartz. We used the same growth conditions here as employed for growth on a $SiO_2$/Si substrate. The best Raman spectrum, with a more enhanced 2D band and a lower D band, was obtained from the 3D-GN grown on the sapphire substrate; this may be attributed to the close match of the sapphire (111) facet with the lattice of graphene, which provides an ideal surface for graphene epitaxy. [42, 43] The direct growth of a 3D-GN on any electronic device-compatible substrate will open up the possibility of producing ready-to-use graphene with minimum defects in the semiconductor industry.

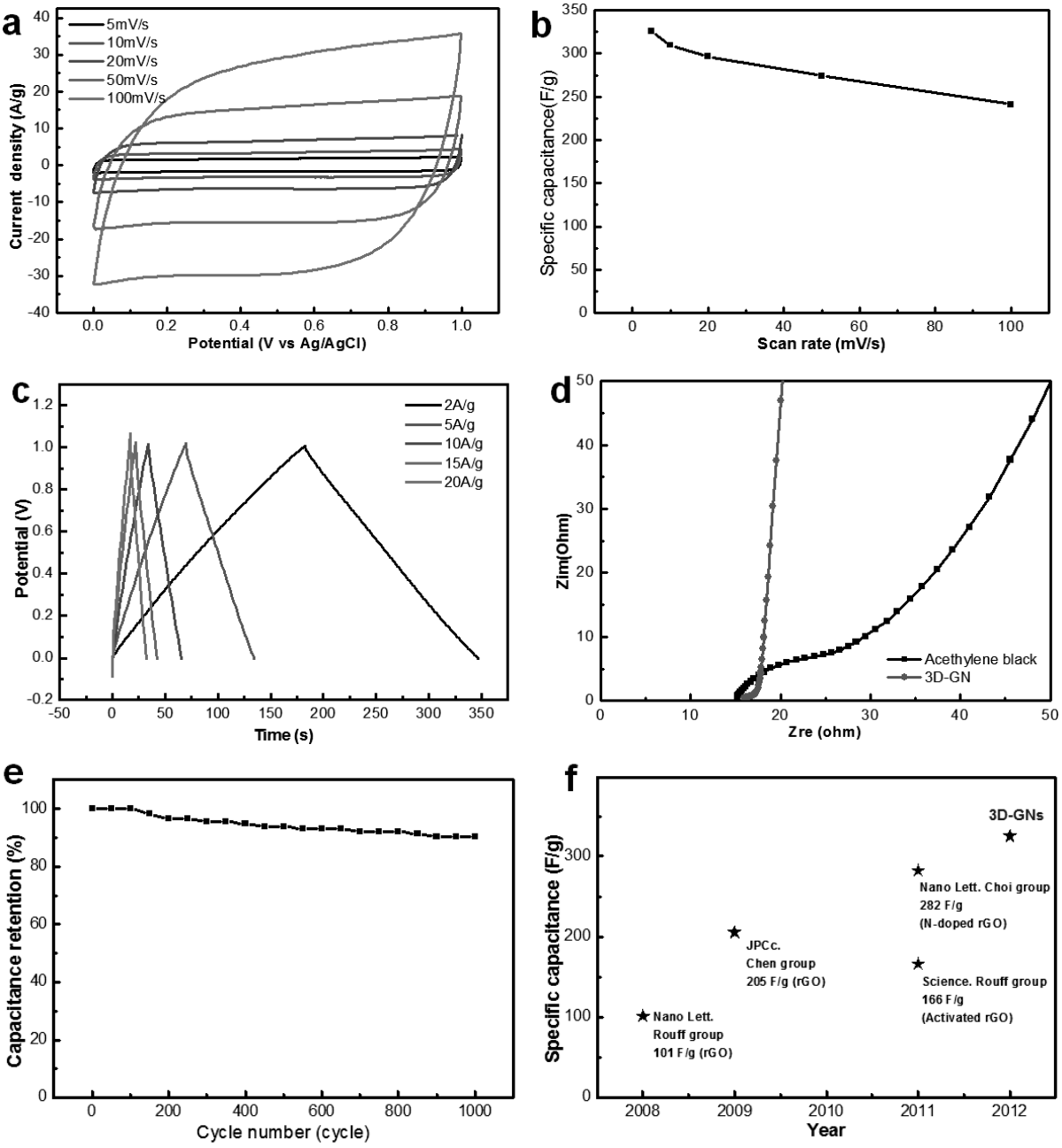


**Figure 12 : Electrochemical performance of 3D-GN-based supercapacitor. (a) Cyclic voltammogram curve at different scan rates. (b) Capacitance change at various scan rates. (c) Charging/discharging curve at different discharge current densities. (d) Nyquist impedance plot. The inset shows a zoomed-in image of the high frequency region. (e) Capacitance retention plot with cycle number. (f) Plot of recorded specific capacitances of EDLC electrodes acquired from various methods.**

As a demonstration of the potential of 3D-GNs, the performance of the 3D-GN sample as an EDLC electrode was studied using cyclic voltammetry (CV) and galvanostatic charge/discharge measurements. Here we used a 3D-GN prepared with a specific surface area of 1,025 $m^2/g$ and conductivity of 12 S/cm fabricated on a bulk scale. The 3D-GN was p-doped by dipping it in a $HNO_3$ solution to further enhance conductivity up to 99 Ω/□. Figure 5a shows the CV results of 3 cell electrodes assembled with 3D-GNs as the active material at various scan rates in a range of 0 V to 1.0 V vs Ag/AgCl. Generally, for a supercapactior that uses a carbon-based electrode, the CV curve shape and the specific capacitance can significantly degrade as the voltage scan rate increases, showing distortion of the rectangular shape. The CV curves of the 3D-GN supercapacitor at all scan rates except the one at the highest scan rate of 100 mV/s were nearly rectangular, indicating that the 3D-GN is an ideal carbon electrode material with excellent capacitance behavior and low contact resistance. A slight deviation from an ideal double-layer capacitor at a scan rate of 100 mV/s could be related to the increased resistance. An outstanding specific capacitance of 325 F/g in a $LiClO_4$ solution was obtained at a scan rate of 5 mV/s, calculated by equation (1). [44]

$$C = \frac{1}{2 \cdot m \cdot \Delta V \cdot v} \int IdV \qquad \textbf{eq 7}$$

The essentially greater specific capacitance of the 3D-GN relative to that of previously reported values for graphene electrode materials (101-282 F/g, as shown in Figure 12f) is attributable to the large accessible surface area achieved by proper-sized mesopores and 3-dimensionally interconnected conducting pathways of graphene. More specifically, compared to several previously reported supercapacitors with high specific surface area greater than 2000 $m^2/g$, which show relatively low capacitance values due to the presence of predominant micro-pores less than 2 nm in diameter, our 3D-GNs have a reasonably great specific surface area of pores with controlled sizes of about 10 nm in diameter which can be effectively and fully used for electrochemical reaction sites.[45, 46] The specific capacitance per unit surface area was as high as 31.7 $F/cm^2$, an outstanding value for double-layer capacitance. Importantly, the capacitance loss of graphene was less than 26 %, with a scan rate variation from 5 to 100 mV/s, as shown in Figure 12b. The galvanostatic charge/discharge method was applied to evaluate the capacitance performance of the 3D-GN. A well symmetric charge/discharge characteristic with a triangular shape distinctive for an ideal capacitor was observed even at a high current load of 20 A/g (Figure 12c).

In order to obtain a comprehensive perspective on the capacitive response, an electrochemical impedance test was conducted. The Nyquist plot of the 3D-GN in Figure 12d exhibits a small semicircle at the high frequency region and a straight line in the medium frequency region. The small diameter of

the semicircle at the high frequency region represents the low charge transfer resistance at the interface between the electrode and electrolyte. The nearly vertical second partial semicircle at the medium frequency region indicates the low charge transfer resistance for the adsorption process, which is greatly affected by the surface morphology of the electrode. The low resistance at both the high and medium frequency regions can be due to improved conductivity in the 3-dimensionally interconnected graphene networks through the nano-channels with proper diameters. The 3D-GN based supercapacitor retains ~ 90% of its performance even after 1000 cycles, suggesting great life-cycle stability of the 3D-GN based electrode materials for their practical use in electrochemical capacitors as shown in Figure 12e.

## 2.4 Conclusions

In conclusion, we developed an easy and direct method for fabricating 3D networks of near single-layer graphene via the CVD technique from a PVA/iron precursor on a bulk scale. Our substrate-free CVD method adds the dimensional tunability to high quality graphene, by enabling the creation of nanonetworks. A 3D-GN can be grown on any inert substrate such as $Al_2O_3$, quartz, or $SiO_2$/Si wafer, etc. and can be further transferred onto any arbitrary substrate for flexible devices, cell culture plates, etc. The ratio of $I_{2D}/I_G$ (= 3.27) for the representative 3D-GN confirms the formation of a near single layer of graphene. A resistance of ~52 S/cm, high surface areas of 1,025 $m^2/g$, and a great porosity of around 3.4 $cm^3/g$ were recorded for the 3D-GN. Electrochemical measurements indeed proved that the high surface area 3D-GN based electrode, which provides easy contact and transportation of both charges and the electrolyte through the 3D conducting pathways, exhibited excellent specific supercapacitance. The outstanding performance of 3D-GNs fabricated with this easy and inexpensive method suggests a straightforward route to achieve nano-textured 3D graphene with strong potential for use in electronic devices and heat-dissipation systems, as well as for energy-related materials.

## 2.5 References


1. Bae, S.; Kim, H.; Lee, Y.; Xu, X.; Park, J.-S.; Zheng, Y.; Balakrishnan, J.; Lei, T.; Ri Kim, H.; Song, Y. I.; Kim, Y.-J.; Kim, K. S.; Ozyilmaz, B.; Ahn, J.-H.; Hong, B. H.; Iijima, S. Roll-to-roll production of 30-inch graphene films for transparent electrodes. *Nat. Nanotech.* 2010, 5, 574-578.
2. Chen, Z. P.; Ren, W. C.; Gao, L. B.; Liu, B. L.; Pei, S. F.; Cheng, H. M. Three-dimensional flexible and conductive interconnected graphene networks grown by chemical vapour deposition. *Nat. Mater.* 10, 424-428.
3. Zhu, Y.; Murali, S.; Stoller, M. D.; Ganesh, K. J.; Cai, W.; Ferreira, P. J.; Pirkle, A.; Wallace, R. M.; Cychosz, K. A.; Thommes, M.; Su, D.; Stach, E. A.; Ruoff, R. S. Carbon-Based Supercapacitors Produced by Activation of Graphene. *Science* 2011, 332, 1537-1541.
4. Jang, J.-H.; Jhaveri, S. J.; Rasin, B.; Koh, C.; Ober, C. K.; Thomas, E. L. Three-Dimensionally-Patterned Submicrometer-Scale Hydrogel/Air Networks That Offer a New Platform for Biomedical Applications. *Nano Lett.* 2008, 8, 1456-1460.
5. Jang, J.-H.; Ullal, C. K.; Gorishnyy, T.; Tsukruk, V. V.; Thomas, E. L. Mechanically Tunable Three-Dimensional Elastomeric Network/Air Structures via Interference Lithography. *Nano Lett.* 2006, 6, 740-743.
6. Jang, J.-H.; Dendukuri, D.; Hatton, T. A.; Thomas, E. L.; Doyle, P. S. A Route to Three-Dimensional Structures in a Microfluidic Device: Stop-Flow Interference Lithography. *Angew. Chem.* 2007, 119, 9185-9189.
7. Zorlutuna, P.; Annabi, N.; Camci-Unal, G.; Nikkhah, M.; Cha, J. M.; Nichol, J. W.; Manbachi, A.; Bae, H.; Chen, S.; Khademhosseini, A. Microfabricated Biomaterials for Engineering 3D Tissues. *Advanced Materials* 2012, 24, 1782-1804.
8. Geim, A. K.; Novoselov, K. S. The rise of graphene. *Nat. Mater.* 2007, 6, 183-191.
9. Novoselov, K. S.; Geim, A. K.; Morozov, S. V.; Jiang, D.; Zhang, Y.; Dubonos, S. V.; Grigorieva, I. V.; Firsov, A. A. Electric Field Effect in Atomically Thin Carbon Films. *Science* 2004, 306, 666-669.
10. Zhang, Y.; Tan, Y.-W.; Stormer, H. L.; Kim, P. Experimental observation of the quantum Hall effect and Berry's phase in graphene. *Nature* 2005, 438, 201-204.
11. Reina, A.; Jia, X.; Ho, J.; Nezich, D.; Son, H.; Bulovic, V.; Dresselhaus, M. S.; Kong, J. Large Area, Few-Layer Graphene Films on Arbitrary Substrates by Chemical Vapor Deposition. *Nano Lett.* 2008, 9, 30-35.
12. Bhaviripudi, S.; Jia, X.; Dresselhaus, M. S.; Kong, J. Role of Kinetic Factors in Chemical Vapor Deposition Synthesis of Uniform Large Area Graphene Using Copper Catalyst. *Nano Lett.* 2010, 10, 4128-4133.
13. Li, X.; Cai, W.; An, J.; Kim, S.; Nah, J.; Yang, D.; Piner, R.; Velamakanni, A.; Jung, I.; Tutuc, E.; Banerjee, S. K.; Colombo, L.; Ruoff, R. S. Large-Area Synthesis of High-Quality and Uniform Graphene Films on Copper Foils. *Science* 2009, 324, 1312-1314.
14. Li, X.; Cai, W.; Colombo, L.; Ruoff, R. S. Evolution of Graphene Growth on Ni and Cu by Carbon Isotope Labeling. *Nano Lett.* 2009, 9, 4268-4272.
15. Cao, X. H.; Shi, Y. M.; Shi, W. H.; Lu, G.; Huang, X.; Yan, Q. Y.; Zhang, Q. C.; Zhang, H. Preparation of Novel 3D Graphene Networks for Supercapacitor Applications. *Small* 7, 3163-3168.
16. Michael Thompson Pettes, H. J., Rodney S. Ruoff, and Li Shi. Thermal Transport in Three-Dimensional Foam Architectures of Few-Layer Graphene and Ultrathin Graphite. *Nano Lett.* 2012, DOI:10.1021/nl300662q.

17. Jeong, H. M.; Lee, J. W.; Shin, W. H.; Choi, Y. J.; Shin, H. J.; Kang, J. K.; Choi, J. W. Nitrogen-Doped Graphene for High-Performance Ultracapacitors and the Importance of Nitrogen-Doped Sites at Basal Planes. *Nano Lett.* 2011, 11, 2472-2477.

18. Choi, B. G.; Yang, M.; Hong, W. H.; Choi, J. W.; Huh, Y. S. 3D Macroporous Graphene Frameworks for Supercapacitors with High Energy and Power Densities. *ACS Nano* 2012, 6, 4020-4028.

19. Yao, Y.; Li, Z.; Lin, Z.; Moon, K.-S.; Agar, J.; Wong, C. Controlled Growth of Multilayer, Few-Layer, and Single-Layer Graphene on Metal Substrates. *J. Phy. Chem. C* 115, 5232-5238.

20. Cherian, C. T.; Giustiniano, F.; Martin Fernandez, I.; Andersen, H.; Balakrishnan, J.; Özyilmaz, B. 'Bubble-Free' Electrochemical Delamination of CVD Graphene Films. *Small* 2015, 11, 189-194.

21. Xue, Y. Z.; Wu, B.; Guo, Y. L.; Huang, L. P.; Jiang, L.; Chen, J. Y.; Geng, D. C.; Liu, Y. Q.; Hu, W. P.; Yu, G. Synthesis of large-area, few-layer graphene on iron foil by chemical vapor deposition. *Nano Res.* 4, 1208-1214.

22. Conway, B. E. *Electrochemical Supercapacitor : Scientific Fundamentals and Technological Applications* Pleum; New York: 1999.

23. Kötz, R.; Carlen, M. Principles and applications of electrochemical capacitors. *Electrochimica Acta* 2000, 45, 2483-2498.

24. Wang, G.; Zhang, L.; Zhang, J. A review of electrode materials for electrochemical supercapacitors. *Chem. Society Reviews* 2012, 41, 797-828.

25. Bose, S.; Kuila, T.; Mishra, A. K.; Rajasekar, R.; Kim, N. H.; Lee, J. H. Carbon-based nanostructured materials and their composites as supercapacitor electrodes. *Journal of Materials Chemistry* 2012, 22, 767-784.

26. Lee, C.; Wei, X.; Kysar, J. W.; Hone, J. Measurement of the Elastic Properties and Intrinsic Strength of Monolayer Graphene. *Science* 2008, 321, 385-388.

27. Stoller, M. D.; Park, S.; Zhu, Y.; An, J.; Ruoff, R. S. Graphene-Based Ultracapacitors. *Nano Lett.* 2008, 8, 3498-3502.

28. Jiang, P.; Bertone, J. F.; Hwang, K. S.; Colvin, V. L. Single-Crystal Colloidal Multilayers of Controlled Thickness. *Chem. of Mater.* 1999, 11, 2132-2140.

29. Babin, P.; Gavrilov, A.; Trofimova, L. Absorption spectra and the nature of complexes in the polyvinyl Alcohol-Nickel (II) chloride system. *J. Appl. Spectro.* 2006, 73, 151-153.

30. Nouh, S. A.; Radwan, M. M.; Agami, W. R.; Morsy, M. Studies on the effect of laser radiation on the thermal stability of stabilized poly(vinyl chloride). *J. Appl. Polym. Sci.* 2003, 89, 2249-2255.

31. Lee, J.-S.; Ahn, H.-J.; Yoon, J.-C.; Jang, J.-H. Three-dimensional nano-foam of few-layer graphene grown by CVD for DSSC. *Phy. Chem. Chem. Phy.* 2012, 14, 7938-7943.

32. Kumar, S.; Chakarvarti, S. K. SEM morphology and XRD characterization of Ni microstructure arrays synthesized by dc electrodeposition in porous polycarbonate templates. *J. Mater. Sci.* 2004, 39, 3249-3251.

33. Grosvenor, A. P.; Kobe, B. A.; Biesinger, M. C.; McIntyre, N. S. Investigation of multiplet splitting of Fe 2p XPS spectra and bonding in iron compounds. *Surf. and Interf. Anal.* 2004, 36, 1564-1574.

34. Suzuki, S.; Yanagihara, K.; Hirokawa, K. XPS study of oxides formed on the surface of high-purity iron exposed to air. *Surf. and Interf. Anal.* 2000, 30, 372-376.

35. Ji, H.; Hao, Y.; Ren, Y.; Charlton, M.; Lee, W. H.; Wu, Q.; Li, H.; Zhu, Y.; Wu, Y.; Piner, R.; Ruoff, R. S. Graphene Growth Using a Solid Carbon Feedstock and Hydrogen. *ACS Nano* 2011, 5, 7656-7661.

36. Mérel, P.; Tabbal, M.; Chaker, M.; Moisa, S.; Margot, J. Direct evaluation of the sp3 content in diamond-like-carbon films by XPS. *Appl. Surf. Sci.* 1998, 136, 105-110.

37. Miyasaka, Y. N., Atsushi; Temmyo, Jiro. Graphite Thin Films Consisting of Nanograins of Multilayer Graphene on Sapphire Substrates Directly Grown by Alcohol Chemical Vapor Deposition. *JPN J. Appl. Phy.* 2011, 50, 04DH12.

38. Song, H. J.; Son, M.; Park, C.; Lim, H.; Levendorf, M. P.; Tsen, A. W.; Park, J.; Choi, H. C. Large scale metal-free synthesis of graphene on sapphire and transfer-free device fabrication. *Nanoscale* 2012, 4, 3050-3054.

39. Yan, J.; Wei, T.; Shao, B.; Fan, Z.; Qian, W.; Zhang, M.; Wei, F. Preparation of a graphene nanosheet/polyaniline composite with high specific capacitance. *Carbon* 2010, 48, 487-493.

40. Jha, N.; Ramesh, P.; Bekyarova, E.; Itkis, M. E.; Haddon, R. C. High Energy Density Supercapacitor Based on a Hybrid Carbon Nanotube–Reduced Graphite Oxide Architecture. *Adv. Energy Mater.* 2012, 2, 438-444.

# CHAPTER 3 : EFFECT OF THE GRAPHENE TRANSFER METHOD ON GRAPHENE -ENHANCED RAMAN SPECTROSCOPY



## 3.1 Introduction

Graphene has been broadly used for chemical and biological sensing because of its superior detection properties due to a high surface area, easy functionalization and stability in ambient environments. Graphene can be synthesized using epitaxial growth[1, 2], mechanical exfoliation[3], chemical methods[4, 5] and chemical vapor deposition (CVD)[6, 7]. Among them, the CVD technique is extensively used to produce thin graphene films since it provides a relatively friendly synthesis route and also produces high quality graphene. In general, graphene films obtained by CVD needs to be transferred to desired substrates for further applications. Several transfer methods such as polymer-assisted[8] (PMMA, PDMS, thermal release tape), polymer-free[9], electrochemical delamination[10, 11] have been used to transfer the graphene films. Polymer-assisted transfer has been widely used due to its easy processing steps. Aside from surface-enhanced Raman scattering (SERS)[12, 13,14] which is one of the most efficient detection tools utilizing metal substrate for a variety of common molecules, graphene-enhanced Raman spectroscopy (GERS)[15, 16] is another efficient technique to increase the Raman scattering of adsorbed probe molecules adsorbed on graphene. The concept of GERS has been widely applied to graphene oxide[5, 17, 18], hydrogen terminated graphene[19], nano-mesh graphene[20] and nitrogen-doped graphene[21]. It has been reported that GERS depends on various factors such as the number of graphene layers[22, 23], the density of the probe molecules[24], the space between graphene and the probe molecule, the Fermi level of graphene, which changes with doping[25-27], an interference effect from the substrate, and molecular alignment[28]. Further, in GERS the contribution of the electromagnetic-enhanced plasmons is in the terahertz range, and Raman signals are solely due to the chemical mechanism (CM) which is closely related to the charge transfer between probe molecules and the graphene substrate. Here, we report the CM properties of graphene grown by CVD can be affected by the methods of transfer (i) PMMA-and (ii) TRT-assisted, by comparing their GERS of R6G probe molecules. To date there are, to the best of our knowledge, no comprehensive reports on the effect of the graphene transfer method on GERS properties. We found that PMMA-transferred graphene, which is more defective, produces high signal intensity in GERS due to the PMMA residues, which cause enhanced charge transfer. A detailed study on graphene (PMMA- and TRT-assisted) was done using XPS measurements, UV-Vis spectroscopy and time decay photoluminescence (PL).

## 3.2 Experimental methods

### 3.2.1. Graphene growth and transfer process

Graphene growth on copper foil (Alfa Aeasr, 99.9999%) was performed by chemical vapor deposition (CVD) at 1000 ºC. First 100sccm of $H_2$ was passed over the foil while increasing the temperature to remove impurities on its surface. Then a continuous flow of 100sccm of $CH_4$ gas was passed through the quartz tube for 5min, without turning off the $H_2$, to grow the graphene. After growth, the temperature in the quartz tube rapidly decreased to room temperature. The graphene transfer processes were as follows. For PMMA-graphene, the graphene/Cu film was coated using a PMMA solution dissolved in toluene and then dried at 100 ºC in an ambient air for 10min. For the preparation of TRT-graphene, the tape was attached to the graphene/Cu film and pressure was then applied to remove air between the tape and sample. For both PMMA- and TRT-graphene, the Cu foil was removed from the sample by etching for 2hrs in an ammonium persulfate solution. After removing the Cu foil, both samples were floated for 1hr on D.I. water to wash the etchant solution from the samples and dried using $N_2$ gas. Finally the prepared sample was transferred onto the desired substrate.

### 3.2.2 R6G dye adsorption on the graphene substrate

R6G as a probe molecule was dissolved in a DI water. The concentration of R6G in solution was $10^{-5}$ M (mol $L^{-1}$). The molecule was adsorbed by soaking the sample in the prepared solution for 1hr followed by washing three times to remove any residue.

### 3.2.3 GERS measurement

To confirm the GERS effects of the prepared substrate, combined AFM-Raman microscopy (WITec) was used to check the signal enhancement of R6G dye. R6G was dissolved in DI water with a concentration of 1 mM to obtain a stock solution and then diluted to obtain the required concentration. The substrate was dipped into the dye solution where it remained for 60 min to stabilize deposition. After adsorption, the substrate was rinsed by DI water. For the Raman measurements, the power was adjusted to 0.2 mW and integration time was set to be 10 s.

### 3.2 Results and discussions

The graphene synthesis procedure is reported elsewhere. Briefly, the surface of a copper foil was acid cleaned and used as a substrate. Graphene growth by CVD was performed in a 2-inch quartz tube at 1000°C using $CH_4/H_2$ gases. The graphene was transferred onto a $SiO_2/Si$ substrate by the two methods, PMMA-assisted and TRT-assisted. These samples are denoted PMMA-graphene and TRT-graphene for the rest of this paper. Details of the sample preparation are discussed in the experimental section. Single-layer graphene was used to avoid any effect caused by multiple layers. Graphene growth conditions (temperature, growth time, pressure) were kept the same for both graphene.

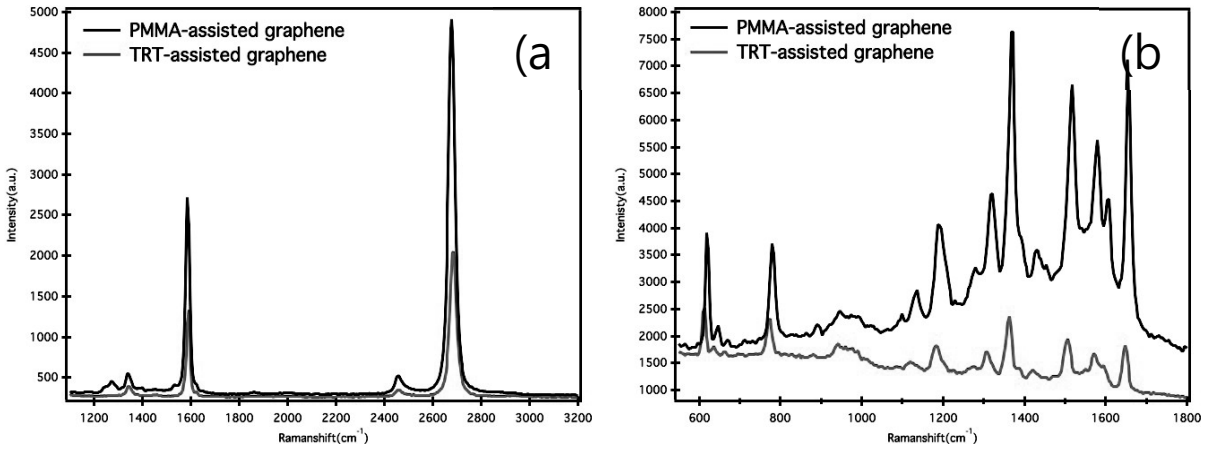


**Figure 13 : (a) The Raman of TRT-assisted graphene (red line), and PMMA-assisted graphene (black line), (b) GERS effects of TRT-assisted graphene (red), and PMMA-assisted graphene (black).**

| | G band($cm^{-1}$) | 2D band($cm^{-1}$) |
|---|---|---|
| **PMMA-graphene** | 1587.03 | 2677.77 |
| **TRT-graphene** | 1590.74 | 2683.33 |

**Table 2. The position of G and 2D band of PMMA and TRT-graphene**

Figure 1a provides Raman spectra of both graphene. The defect-band (or D-band peak) at 1350 $cm^{-1}$ was present in both cases. The G band and 2D band position are 1587.03 $cm^{-1}$, 2677.77 $cm^{-1}$ for the PMMA-graphene and 1590.74 $cm^{-1}$, 2683.33 $cm^{-1}$ for the TRT-graphene, implying hole-doping properties in both samples (G and 2D band positions are 1580 $cm^{-1}$ and 2670 $cm^{-1}$ for pristine graphene). The positions of both the G and 2D bands are upshifted for hole-doped graphene, while electron-doped graphene has a downshift in the G band and an upshift in the 2D band. Oxygen-containing groups such as epoxy, ether, or carboxyl on the graphene surface act as hole-acceptors which shift the Fermi level and cause an upshift of the G and 2D peaks, as shown in Figure 13(a). Residues from PMMA or TRT can change the pristine graphene to hole-doped graphene, because oxygen in the air easily combines with any residue[29]. It is known that chemical residues on the surface of transferred graphene are inevitable despite a number of efforts to remove any unintentional impurity on the surface[30]. Besides, the annealing process used to remove the polymer residue induces the attachment of oxygen molecules to the graphene and a rehybridization of carbon atoms from $sp^2$ to $sp^3$ bonds, as can be seen from UV absorbance results (Figure 14(a)). Notably, the G and 2D peak positions of TRT-graphene were slightly more upshifted than for PMMA-graphene. The degree of upshift in band positions tells us that TRT-graphene has more hole-doping properties than PMMA-graphene. In general, hole-doped graphene has a higher GERS enhancement than electron-doped graphene because the Fermi level of graphene shifts below the Dirac point and charge transfer is enhanced because the down-shifted Fermi level makes the energy gap between the LUMO of the probe molecules and graphene closer to the energy of the laser used, giving a higher chance of electron excitation[26]. However, Figure 1b shows that all the GERS spectra peaks of the R6G probe on PMMA-graphene are higher than those on the more hole-doped TRT-graphene. In our experiments, the 532 nm laser power was kept at 0.2 mW, which produces neither local defects in graphene (which are caused by high laser power) nor the possibility of misinterpreting the GERS signal because the resonance Raman scattering of R6G lies in the visible wavelength range. Besides, since the concentration of R6G is a major factor, in addition to the incident laser power used to characterize the samples, the R6G concentration was fixed at around 10μM which does not cause R6G to aggregate on the graphene surface. The comparative peak positions of PMMA-graphene and TRT-graphene are shown in table 2. In Figure 13(b), the distinct Raman peak at 1650 $cm^{-1}$, which is attributed to the aromatic mode in the R6G dye, is six times higher on PMMA-graphene than on TRT-graphene. This implies that the charge transfer between R6G molecules and PMMA-graphene is much easier than for TRT-graphene

which may be attributed to the simple arrangement of probe molecules on the PMMA-graphene surface[31]. This observation is in disagreement with the above argument on GERS intensity based on the hole-doping properties of graphene. While TRT-graphene has more hole-doping properties than PMMA-graphene, the GERS of TRT-graphene is lower. To address this discrepancy, we performed optical property measurements on both samples. Figure 14 (a) shows the UV-absorbance results of R6G molecules on graphene prepared by the two transfer methods, with all other preparation parameters the same. The characteristic absorbance peak at 520 nm of the dye molecules on PMMA-graphene was much broader than for the TRT-graphene due to band splitting, implying transitions at both higher and lower energy induced by the formation of aggregated dyes[32]. Furthermore, R6G/PMMA-graphene showed a higher contribution of C-C bonds at 265 nm than R6G/TRT-graphene, indicating that the π–π* interaction between PMMA-graphene and the probe molecules is stronger than for TRT-graphene[33]. Figure 14(b) revealed another important difference in the Raman peaks. After adsorbing R6G dye on each graphene substrate, the Raman intensity was greatly reduced and the 2D position of both graphenes was upshifted compared to samples without the adsorbing dye. The 2D positions of PMMA- and TRT-graphenes were respectively upshifted by 15.74 $cm^{-1}$ and 4.9 $cm^{-1}$ compared to samples before dye deposition, implying PMMA-graphene had more hole-doping properties after dye adsorption. It has been reported that intensity weakening and a position shift of the 2D peak of graphene occur as a result of doping because electron-electron scattering becomes competitive with electron-phonon scattering[34]. Therefore, the more significant hole doping properties in PMMA-graphene after dye adsorption are likely due to the larger amount of dye[24] having much greater π–π* interaction and this may explain the higher GERS enhancement of R6G dye on PMMA-graphene.

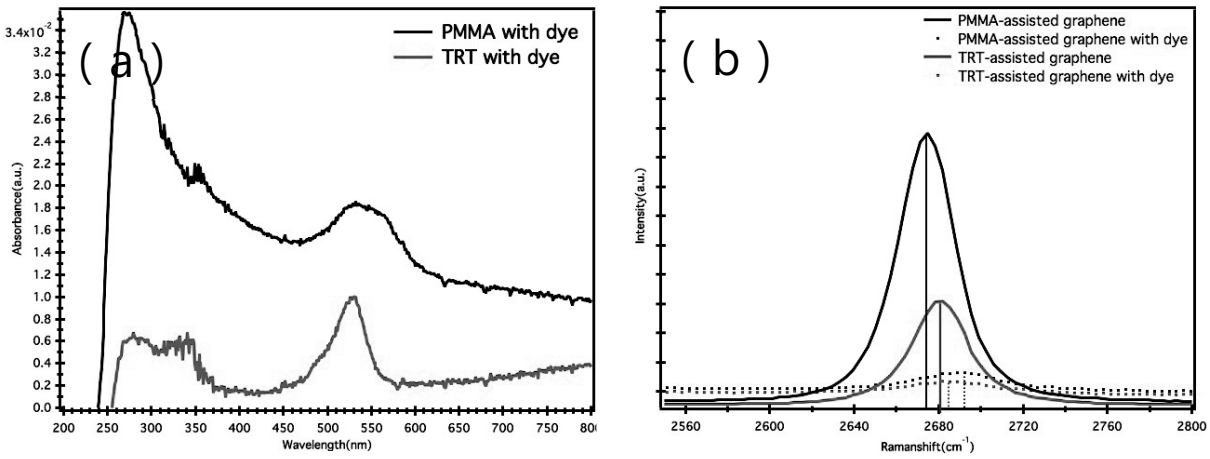


**Figure 14. (a) UV-absorbance of Dye/TRT-graphene/quartz (red color) and Dye/PMMA-graphene/quartz (black color) (b) 2D peak of PMMA-assisted (black) and TRT-assisted graphene(red) before (dot) and after (line) dye absorption.**

In order to further explore the effects of molecular arrangements on charge transfer, the functional groups on the graphene surface were characterized by x-ray photoelectron spectroscopy. The detailed XPS results of PMMA-and TRT-graphene in Figure 15, fitted using Casa XPS software, confirmed the presence of a large number of oxygen-containing groups such as C-O, COOH in both samples. In Figure 15(a), C-C, C-O and COOH in PMMA-graphene appeared with percentages of 59.85 %, 27.90 % and 12.25 %, respectively. Figure 15(b) denotes the XPS data of TRT-graphene with C-C, C-O and COOH percentages of 55.31 %, 38.40 % and 6.29 %, respectively. COOH groups on the surface of PMMA-graphene are detected to have twice the concentration of those on TRT-graphene while the amount of epoxy/ether groups (C-O) is lower than for TRT-graphene. It can be inferred that either COOH or C-O on the surface of graphene affected the orientation of R6G and thus its π–π* interaction with the graphene surface[35]. It has been reported that Coulombic interactions between the negatively charged COOH groups in GO and the positively charged R6G dye molecule[36, 37] allow firm binding between the substrate and the probe molecules[38, 39]. Furthermore, carboxyl groups, mainly located at the edges of the graphene surface do not interfere with the π-π* stacking of R6G dye molecules on the graphene surface. On the other hand, the epoxy/ether groups that reside on the planar surface of graphene tend to restrict π–π* interactions between the graphene surface and R6G. Consequently, the R6G molecules are preferentially positioned at C-C sites on the surface of a graphene that has a larger amount of COOH groups and fewer C-O groups. The arrangement of R6G molecules on the surface of PMMA-graphene leads to strong π-π* interactions in the region where epoxy/ether groups are absent. As a result, the density of R6G molecules on the surface of PMMA-graphene was higher than on TRT-graphene, leading to a higher UV-absorbance peak intensity (Figure 15a) and more hole-doping properties (Figure 15b).

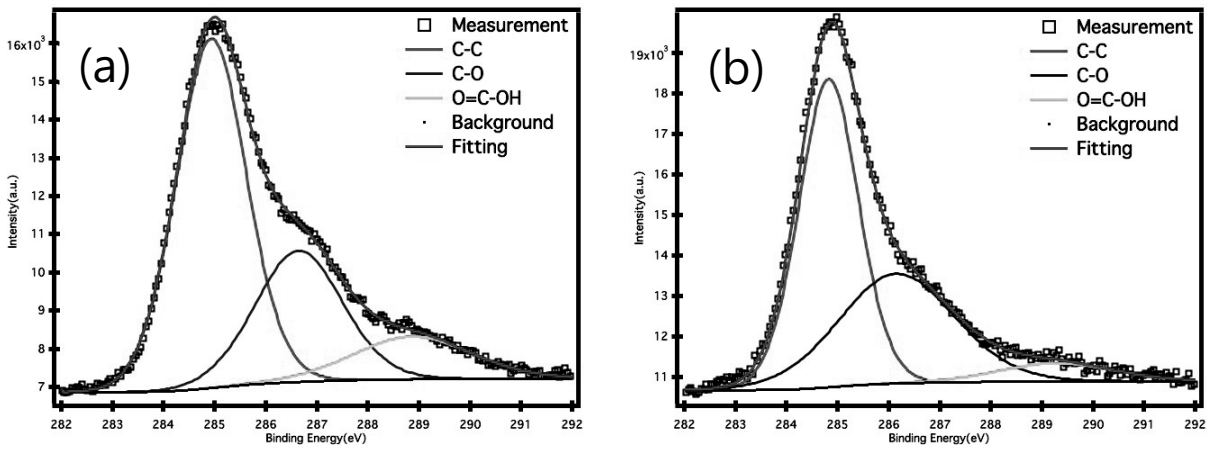


**Figure 15 : XPS data of (a) PMMA-transferred graphene & (b) TRT- transferred graphene**

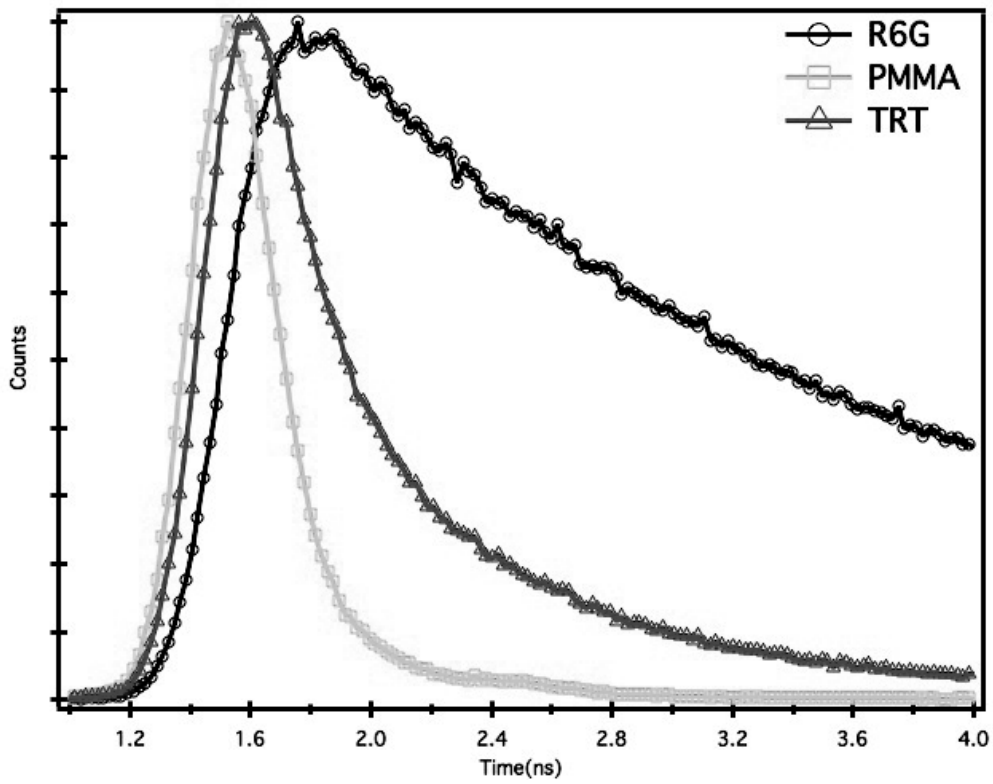


**Figure 16 : Fluorescence decays of PMMA-assisted graphene (cyan), TRT-assisted graphene (blue), R6G on SiO2/Si substrate (black line).**

In order to confirm the greater GERS on PMMA-graphene, we have conducted fluorescence decay measurements of the samples using a fluorescence lifetime (PL) spectrometer (Edinburgh Instruments (Model number: FL920)) as shown in Figure 16. The fluorescence decay time measurements give direct evidence of electron transfer between the dye and graphene. The fluorescence decay lifetimes of the samples were calculated using

$$\frac{n^*(t)}{n^*(0)} = e^{\frac{-t}{\tau}} \qquad \text{eq 8}$$

Where is the number of excited elements at time t , is the number of excited elements at time t = 0 , and is lifetime. The fluorescence lifetimes of R6G on PMMA-graphene/quartz, TRT-graphene/quartz, and quartz were calculated to be 0.234, 0.534, 2.44 ns, respectively (Figure 14a). R6G dye molecules on quartz showed the longest lifetime of 2.44 ns, which is slightly lower than the reported value of 3.8 ns, implying a lower concentration of dye molecules in the solution-based measurement conditions than in the substrate-based measurement ones. The one order of magnitude lower fluorescence lifetime of R6G on both the TRT-and PMMA-substrates compared to R6G indicates fast charge transfer between the dye and the graphene films, which supports the reason for the larger Raman scattering signals of R6G observed on the surface of graphene than on the $SiO_2$/Si substrate. Importantly, the PL lifetime for R6G/PMMA-graphene was half that for R6G/TRT-graphene, indicating the best charge transfer among the three samples. This is in good agreement with the 6 times greater GERS signal on PMMA-graphene than on TRT-graphene and bare quartz.

### 3.3 Conclusion

We report effects of the graphene transfer method on GERS is quite well explained by charge transfer properties between dye molecules and the graphene substrate. Our results shows PMMA-assisted graphene has high GERS enhancement up to 6 times than the TRT-assisted graphene. It is substantially attributed to the presence of strong π–π interaction and more carboxyl groups in PMMA-transferred graphene, which were proved by XPS results. Our results indicate the need for a much closer look of GERS enhancement in graphene dependent on functional groups and doping which are not the same for the different transfer methods.

### 3.4 References

1. Gao, L.; Guest, J. R.; Guisinger, N. P. Epitaxial Graphene on Cu(111). *Nano Letters* 2010, 10, 3512-3516.

2. Sutter, P. W.; Flege, J.-I.; Sutter, E. A. Epitaxial graphene on ruthenium. *Nature Materials* 2008, 7, 406-411.

3. Novoselov, K. S.; Geim, A. K.; Morozov, S. V.; Jiang, D.; Zhang, Y.; Dubonos, S. V.; Grigorieva, I. V.; Firsov, A. A. Electric field effect in atomically thin carbon films. *Science* 2004, 306, 666-669.

4. Park, S.; Ruoff, R. S. Chemical methods for the production of graphenes. *Nature Nanotechnology* 2009, 4, 217-224.

5. Hummers Jr, W. S.; Offeman, R. E. Preparation of Graphitic Oxide. *Journal of the American Chemical Society* 1958, 80, 1339-1339.

6. Li, X.; Magnuson, C. W.; Venugopal, A.; Tromp, R. M.; Hannon, J. B.; Vogel, E. M.; Colombo, L.; Ruoff, R. S. Large-Area Graphene Single Crystals Grown by Low-Pressure Chemical Vapor Deposition of Methane on Copper. *Journal of the American Chemical Society* 2011, 133, 2816-2819.

7. Li, X.; Cai, W.; An, J.; Kim, S.; Nah, J.; Yang, D.; Piner, R.; Velamakanni, A.; Jung, I.; Tutuc, E.; Banerjee, S. K.; Colombo, L.; Ruoff, R. S. Large-area synthesis of high-quality and uniform graphene films on copper foils. *Science* 2009, 324, 1312-1314.

8. Kang, J.; Shin, D.; Bae, S.; Hong, B. H. Graphene transfer: key for applications. *Nanoscale* 2012, 4, 5527-37.

9. Lin, W.-H.; Chen, T.-H.; Chang, J.-K.; Taur, J.-I.; Lo, Y.-Y.; Lee, W.-L.; Chang, C.-S.; Su, W.-B.; Wu, C.-I. A direct and polymer-free method for transferring graphene grown by chemical vapor deposition to any substrate. *ACS nano* 2014, 8, 1784-1791.

10. Wang, Y.; Zheng, Y.; Xu, X.; Dubuisson, E.; Bao, Q.; Lu, J.; Loh, K. P. Electrochemical delamination of CVD-grown graphene film: toward the recyclable use of copper catalyst. *ACS nano* 2011, 5, 9927-9933.

11. Cherian, C. T.; Giustiniano, F.; Martin Fernandez, I.; Andersen, H.; Balakrishnan, J.; Özyilmaz, B. 'Bubble-Free' Electrochemical Delamination of CVD Graphene Films. *Small* 2015, 11, 189-194.

12. Fleischmann, M.; Hendra, P. J.; McQuillan, A. J. Raman spectra of pyridine adsorbed at a silver electrode. *Chemical Physics Letters* 1974, 26, 163-166.

13. Blackie, E. J.; Le Ru, E. C.; Etchegoin, P. G. Single-molecule surface-enhanced Raman spectroscopy of nonresonant molecules. *Journal of the American Chemical Society* 2009, 131, 14466-14472.

14. Stiles, P. L.; Dieringer, J. A.; Shah, N. C.; Van Duyne, R. P. Surface-enhanced Raman spectroscopy. *Annual Review of Analytical Chemistry* 2008, 1, 601-626.

15. Ling, X.; Xie, L.; Fang, Y.; Xu, H.; Zhang, H.; Kong, J.; Dresselhaus, M. S.; Zhang, J.; Liu, Z. Can Graphene be used as a Substrate for Raman Enhancement? *Nano letters* 2009, 10, 553-561.

16. Schedin, F.; Lidorikis, E.; Lombardo, A.; Kravets, V. G.; Geim, A. K.; Grigorenko, A. N.; Novoselov, K. S.; Ferrari, A. C. Surface-Enhanced Raman Spectroscopy of Graphene. *ACS nano* 2010, 4, 5617-5626.

17. Yu, X.; Cai, H.; Zhang, W.; Li, X.; Pan, N.; Luo, Y.; Wang, X.; Hou, J. G. Tuning Chemical Enhancement of SERS by Controlling the Chemical Reduction of Graphene Oxide Nanosheets. *ACS nano* 2011, 5, 952-958.

18. Zhang, L.; Jiang, C.; Zhang, Z. Graphene oxide embedded sandwich nanostructures for enhanced Raman readout and their applications in pesticide monitoring. *Nanoscale* 2013, 5, 3773-9.

19. Lee, J. H.; Lee, E. K.; Joo, W. J.; Jang, Y.; Kim, B. S.; Lim, J. Y.; Choi, S. H.; Ahn, S. J.; Ahn, J. R.; Park, M. H.; Yang, C. W.; Choi, B. L.; Hwang, S. W.; Whang, D. Wafer-scale growth of single-crystal monolayer graphene on reusable hydrogen-terminated germanium. *Science* 2014, 344, 286-9.

20. Liu, J.; Cai, H.; Yu, X.; Zhang, K.; Li, X.; Li, J.; Pan, N.; Shi, Q.; Luo, Y.; Wang, X. Fabrication of Graphene Nanomesh and Improved Chemical Enhancement for Raman Spectroscopy. *J.Phys.Chem.C* 2012, 116, 15741-15746.

21. Lv, R.; Li, Q.; Botello-Mendez, A. R.; Hayashi, T.; Wang, B.; Berkdemir, A.; Hao, Q.; Elias, A. L.; Cruz-Silva, R.; Gutierrez, H. R.; Kim, Y. A.; Muramatsu, H.; Zhu, J.; Endo, M.; Terrones, H.; Charlier, J. C.; Pan, M.; Terrones, M. Nitrogen-doped graphene: beyond single substitution and enhanced molecular sensing. *Sci Rep* 2012, 2, 586.

22. Ling, X.; Wu, J.; Xie, L.; Zhang, J. Graphene-Thickness-Dependent Graphene-Enhanced Raman Scattering. *The Journal of Physical Chemistry* 2013, 117, 2369-2376.

23. Kuo, C.-C.; Chen, C.-H. Graphene thickness-controlled photocatalysis and surface enhanced Raman scattering. *Nanoscale* 2014, 6, 12805-12813.

24. Voggu, R.; Das, B.; Rout, C. S.; Rao, C. N. R. Effects of charge transfer interaction of graphene with electron donor and acceptor molecules examined using Raman spectroscopy and cognate techniques. *Journal of Physics: Condensed Matter* 2008, 20, 472204.

25. Park, C. S.; Zhao, Y.; Lee, J.-H.; Whang, D.; Shon, Y.; Song, Y.-H.; Lee, C. J. Tunable bandgap of a single layer graphene doped by the manganese oxide using the electrochemical doping. *Applied Physics Letters* 2013, 102, 032106.

26. Xu, H.; Xie, L.; Zhang, H.; Zhang, J. Effect of Graphene Fermi Level on the Raman Scattering Intensity of Molecules on Graphene. *ACS nano* 2011, 5, 5338-5344.

27. Hao, Q.; Morton, S. M.; Wang, B.; Zhao, Y.; Jensen, L.; Jun Huang, T. Tuning surface-enhanced Raman scattering from graphene substrates using the electric field effect and chemical doping. *Applied Physics Letters* 2013, 102, 011102.

28. Ling, X.; Wu, J.; Xu, W.; Zhang, J. Probing the Effect of Molecular Orientation on the Intensity of Chemical Enhancement Using Graphene-Enhanced Raman Spectroscopy. *Small* 2012, 8, 1365-1372.

29. Pirkle, A.; Chan, J.; Venugopal, A.; Hinojos, D.; Magnuson, C. W.; McDonnell, S.; Colombo, L.; Vogel, E. M.; Ruoff, R. S.; Wallace, R. M. The effect of chemical residues on the physical and electrical properties of chemical vapor deposited graphene transferred to SiO2. *Applied Physics Letters* 2011, 99, 122108.

30. Lin, Y.-C.; Lu, C.-C.; Yeh, C.-H.; Jin, C.; Suenaga, K.; Chiu, P.-W. Graphene Annealing: How Clean Can It Be? *Nano Letters* 2011, 12, 414-419.

31. Yang, H.; Hu, H.; Ni, Z.; Poh, C. K.; Cong, C.; Lin, J.; Yu, T. Comparison of surface-enhanced Raman scattering on graphene oxide, reduced graphene oxide and graphene surfaces. *Carbon* 2013, 62, 422-429.

32. Thrall, E. S.; Crowther, A. C.; Yu, Z.; Brus, L. E. R6G on graphene: high Raman detection sensitivity, yet decreased Raman cross-section. *Nano Lett* 2012, 12, 1571-7.

33. Xu, Y.; Bai, H.; Lu, G.; Li, C.; Shi, G. Flexible Graphene Films via the Filtration of Water-Soluble Noncovalent Functionalized Graphene Sheets. *Journal of the American Chemical Society* 2008, 130, 5856-5857.

34. Basko, D. M.; Piscanec, S.; Ferrari, A. C. Electron-electron interactions and doping dependence of the two-phonon Raman intensity in graphene. *Physical Review B* 2009, 80, 165413.

35. Balapanuru, J.; Yang, J.-X.; Xiao, S.; Bao, Q.; Jahan, M.; Polavarapu, L.; Wei, J.; Xu, Q.-H.; Loh, K. P. A graphene oxide-organic dye ionic complex with DNA-sensing and optical-limiting properties. *Angewandte Chemie International Edition* 2010, 49, 6549-6553.

36. Mohanty, N.; Berry, V. Graphene-Based Single-Bacterium Resolution Biodevice and DNA Transistor: Interfacing Graphene Derivatives with Nanoscale and Microscale Biocomponents. *Nano Letters* 2008, 8, 4469-4476.

37. Wang, X.; Zhong, S.; He, Y.; Song, G. A graphene oxide – rhodamine 6G nanocomposite as turn-on fluorescence probe for selective detection of DNA. *Analytical Methods* 2012, 4, 360-362.

38. Liang, Y.; Wu, D.; Feng, X.; Müllen, K. Dispersion of Graphene Sheets in Organic Solvent Supported by Ionic Interactions. *Advanced Materials* 2009, 21, 1679-1683.

39. Ren, H.; Kulkarni, D. D.; Kodiyath, R.; Xu, W.; Choi, I.; Tsukruk, V. V. Competitive Adsorption of Dopamine and Rhodamine 6G on the Surface of Graphene Oxide. *ACS Appl. Mater. Interfaces* 2014, 6, 2459-2470.

# CHAPTER 4 : LOTUS LEAF-INSPIRED CVD GROWN GRAPHENE FOR A WATER REPELLANT FLEXIBLE TRANSPARENT ELECTRODE



## 4.1 Introduction

Graphene, two dimensional sheets of carbon atoms, has drawn a lot of attention due to its outstanding properties. In addition to the well-known superior properties of graphene such as high electrical/thermal conductivity, excellent mechanical strength, and optical transparency[1-4], water repellency would be important in applications such as transparent electrodes in various non-wetting electronic devices as well as self-cleaning, anti-fogging, and anti-corrosive materials. In the past few years, researchers have sought to obtain hydrophobic graphene[5-7] surfaces by utilizing low surface energy of graphene along with appropriate roughness. For example, a reduced graphene oxide paper has been shown to have artificial superhydrophobic properties with a contact angle of 150$^{o}$, achieved by an appropriate chemical composition and its stacked geometric features[8, 9]. However, no studies involving CVD-grown graphene[10-12] with lotus leaf-like superhydrophobic properties as well as appropriate conductivity have been reported to date. This is likely due to the difficulties in construction of complex dual-scale roughness with the chosen dimensions (micro/nanoscale) using 2D graphene sheets deposited on planar metal films. Furthermore, from recent research on the wettability of graphene[13], a thin layer of graphene shows wetting transparency due to the atomic-scale thickness of graphene; this indicates that it would be difficult to alter the wettability of many hydrophilic semiconductor-compatible flat substrates, such as $SiO_2$ or GaN, by covering these substrates with a few layers of graphene. At least 4-6 layers of graphene are required to lend a hydrophobic property to the flat surface of the underlying substrate. However, the intrinsic conductivity of the graphene is reduced with increasing thickness. As such, realizing a hydrophobic film with high conductivity for application to a transparent conducting electrode with a water repellant property presents a significant challenge. In fact, the experimentally obtained static contact angle (CA) of epitaxial graphene is only 92$^{o}$, which is slightly hydrophobic; in contrast, an irregular stack of reduced graphene oxide achieved by surface roughness due to the micro/nanopores existing between the layers has a higher CA of 127$^{o}$.[14] Therefore, in order to realize superperhydrophobic devices based on graphene, it is crucial to couple more suitable surface roughness with low surface energy of graphene.

Among many graphene synthesis approaches, CVD growth is a promising method for creating high quality and large scale graphene on a wide range of substrates. The CVD growth of graphene on Cu foil is particularly favored because it allows the creation of optimized graphene with controllable thickness and excellent conductivity. One possible issue related to CVD graphene growth on Cu foil in terms of surface roughness is that the morphology of single-crystalline graphene is limited to the 2D plane of the surface of flat Cu films. Finding ways to create graphene that allow for various shapes and

dimensional scalability while retaining its original conductivity in the form of 2D plane sheets could be important in the realization of future applications of graphene in non-wetting electronic devices where the device is protected from water contact. From this point of view, copper oxide can provide an adequate pathway for morphological change of a copper substrate via an oxidation state change from Cu (0)→ CuO (II), $Cu_2O$ (I).[15-17] In addition, thermal reduction of metal oxides using hydrogen, which has a well understood mechanism,[18] has been frequently used to fabricate active metal catalysts, allowing for further morphological change. We hypothesized that the controlled synthesis of a well-defined metal oxide and metal structure can provide a route to the creation of tailored shapes of graphene via tunable shape of a copper catalyst.

Here, we present, for the first time to the best of our knowledge, a straightforward and simple method to mimic the features of a lotus leaf on the surface of CVD grown graphene via an oxidation state change of a Cu substrate associated with a morphological change during a cycle of high temperature annealing and cooling. The controlled synthesis of well-defined CuO and thus systematically reduced Cu presents an ideal nucleation surface for graphene growth and defines the final shape of 3D graphene structures. Versatile morphology of 3D graphene from flower-like near the flat surface to nano-porous 3D frames can be realized according to the oxidation conditions of Cu and the reduction conditions of CuO coupled with the subsequent growth conditions of graphene. The 3D graphene nanostructure was confirmed to provide comparable performance to that of a 2D single layer graphene, thus offering excellent potential as a 3D transparent electrode. The sheet resistance of graphene on $SiO_2$ was recorded as 400 Ω/□, with an additional super-hydrophobic property based on a contact angle of 170$^o$ triggered by the lotus leaf-like surface and low surface energy of graphene. As a proof of concept, we have fabricated a flexible water-repellent transparent electrode by transferring 3D graphene with a lotus leaf-inspired nano-structure onto a hydrophobic PDMS substrate.

### 4.2 Experimental methods

#### 4.2.1. Synthesis of CuO

The Cu foil was cleaned in acetone and deionized water for 10 min using an ultrasonic generator and then thermal-treated at various temperatures.

#### 4.2.2. Chemical Vapor Deposition of Graphene on 3D Cu

The samples were placed in quartz tube (Scientech Co.) and temperature in heat-zone was increased up to 1000 $^o$C with $H_2$ under the pressure of 0.90 torr. When temperature reached at 1000 $^o$C, the heat-zone was moved to the sample. Then the temperature decreased to 740 $^o$C and the temperature was increased up to 1000 $^o$C. After reaching 1000 $^o$C, the temperature at heat-zone was maintained for 30 min to reduce from CuO to Cu. Then, $CH_4$ gas was flowed with 24 sccm for 25 min under the pressure of 1.0 torr. Finally, the sample was rapidly cooled down to room temperature with flowing $H_2$ and $CH_4$ under the pressure of 1.0 torr.

#### 4.2.3. Transfer of Graphene

PDMS precursors were prepared using the SYLGARD 184 Silicone Elastomer kit. The SYLGARD 184 Silicon Elastomer was mixed with Curing agent at 10 parts to 1 part ratio (10:1). The mixed sample was roll-mixed for 30 min. The graphene on Cu was molded by PDMS and air-bubbles in the sample were removed in a vacuum oven for 1 hr. Then PDMS/graphene/Cu was baked at 80 $^{o}$C for 4 hrs in the oven. In succession, fully cured PDMS/Graphene/Cu sample were floated on aqueous solution of 1 M ammonium persulfate for 2 hrs to remove Cu foil. Lastly, the resulting samples were heat-treated at 80 $^{o}$C to recover the original hydrophobicity deteriorated by the immersion in harsh hydrophilic solutions.

#### 4.2.4. Characterizations

The morphology of the samples was characterized by Field-Emission SEM (Nova Nano-SEM 230, 15 kV). The quality of graphene was determined by Raman spectroscopy (WITec, alpha300R, excited by a 532nm laser). The sheet resistances of the samples transferred onto Si wafer were characterized by 4 point-probe (Dasol Eng, FPP-RS8, pin-spacing 1 mm, pin-radius 100 m). The contact angle was measured by a Drop Shape Analysis System DSA100 (Kruss, Germany). The crystal structure of samples was confirmed with a Rigaku Co. High Power X-Ray Diffractometer D/MAZX 2500V/PC from 10$^{o}$ to 80$^{o}$. Thermal treatment was implemented by a Lenton 1200℃ vacuum tube furnace.

### 4.3 Results and discussion

Figure 1a illustrates the simple two step fabrication process to realize 3D morphology on a Cu substrate. First, a commercially available copper foil that has been widely used for graphene synthesis is heated to 400 $^{o}$C for 2hr under an air atmosphere. The annealing of the Cu foil in the air condition induces partly aggregated metal precursors on the surface of the Cu foil followed by an oxidization reaction of the Cu substrate, resulting in the formation of CuO nanowhiskers protruding from the copper surface. It has been reported that the diameter and height of the nanowhiskers can be controlled by the annealing conditions. Briefly, longer and greater diameter nanowires are obtained with increasing annealing temperature. Second, the CuO nanowhisker structure is again heated to 1000 $^{o}$C under hydrogen conditions for 30 min followed by cooling back to room temperature, which leads to the creation of modified 3D networks (hierarchical structures) on Cu substrates with various morphologies. Figures 1b-1d show SEM images of copper foil at each oxidation state and corresponding XRD results of the samples above. Commercial copper foils have a textured surface with a polycrystalline nature, as shown in Figure 1b. A directional texture with parallel lines with spacing ranging from a few to tens of micrometers and grain boundaries across the film surface is clearly seen in the SEM image. Generally, the surface of copper is further roughened(?) through the surface reconstruction process during high-temperature annealing and growth. The SEM and XRD data of Cu foil after normal graphene growth are presented in the Supporting Information (Figure SX). Figure 1c shows the morphological change of

the flat copper foil into clearly distinguishable nanowhiskers due to the formation of oxidized copper crystals after heat treatment under an oxygen environment. The diameters and the lengths of vertically aligned nanowhiskers on the underlying Cu substrate are set to range from 20 to 50 nm and up to 10 um, respectively, to define the final morphology of graphene. The inset shows a TEM image of an individual CuO nanowhisker and its SAED pattern indexed to the diffraction spots of monoclinic CuO. The XRD spectrum with one strong peak of Cu (0) at 50$^{o}$ and cubic CuO (II) monoclinic phase with a small amount of crystalline $Cu_2O$ further confirms the growth of CuO on the surface of Cu. It has been reported that among the three oxidation states (CuO, $Cu_4O_3$, and $Cu_2O$), CuO and $Cu_2O$ are the more stable compounds. Here, we targeted CuO rather than $Cu_2O$ as a precursor of the Cu catalyst for graphene growth by controlling heating parameters since CuO is more easily reducible than $Cu_2O$ due to its lower activation energy for reduction (15 and 27 kcal/mol, respectively). Another reason for choosing CuO over $Cu_2O$ is that the melting point of CuO is greater than that of $Cu_2O$ (1446 $^{o}$C and 1235 $^{o}$C, respectively), which permits a more sustainable shape during the process of reduction into Cu. A solid peak at 50$^{o}$, which is the same position as the strongest peak of Cu, reveals the existence of unoxidized underlying Cu substrate. Figure 17(d) shows the SEM and XRD results of a representative reduced Cu sample taken immediately after annealing under a hydrogen condition (before the growth of graphene starts). Previous reports reveal that CuO and $Cu_2O$ can be reduced at temperature above 200℃ by thermal processing in $H_2$ conditions. Related studies illustrate that O vacancies created by embedding hydrogen into the lattice of the metal oxide are important in the metal oxide reduction mechanism. Our CuO NWs were reduced to metallic Cu at 1000℃ under a $H_2$ gas in order to verify complete reduction of the CuO. As shown in Figure 1d, XRD confirms that the CuO is completely returned to Cu with a nearly single crystal nature. Importantly, during the high temperature annealing, copper oxide nanowhiskers undergo clear morphological changes through disturbance of their alignment. This leads to the collapse and coalescence of the neighbouring sharp tips, often resulting in double hierarchical bumps, and thus indicating the possibility of the creation of tailored shapes of 3D copper structures.

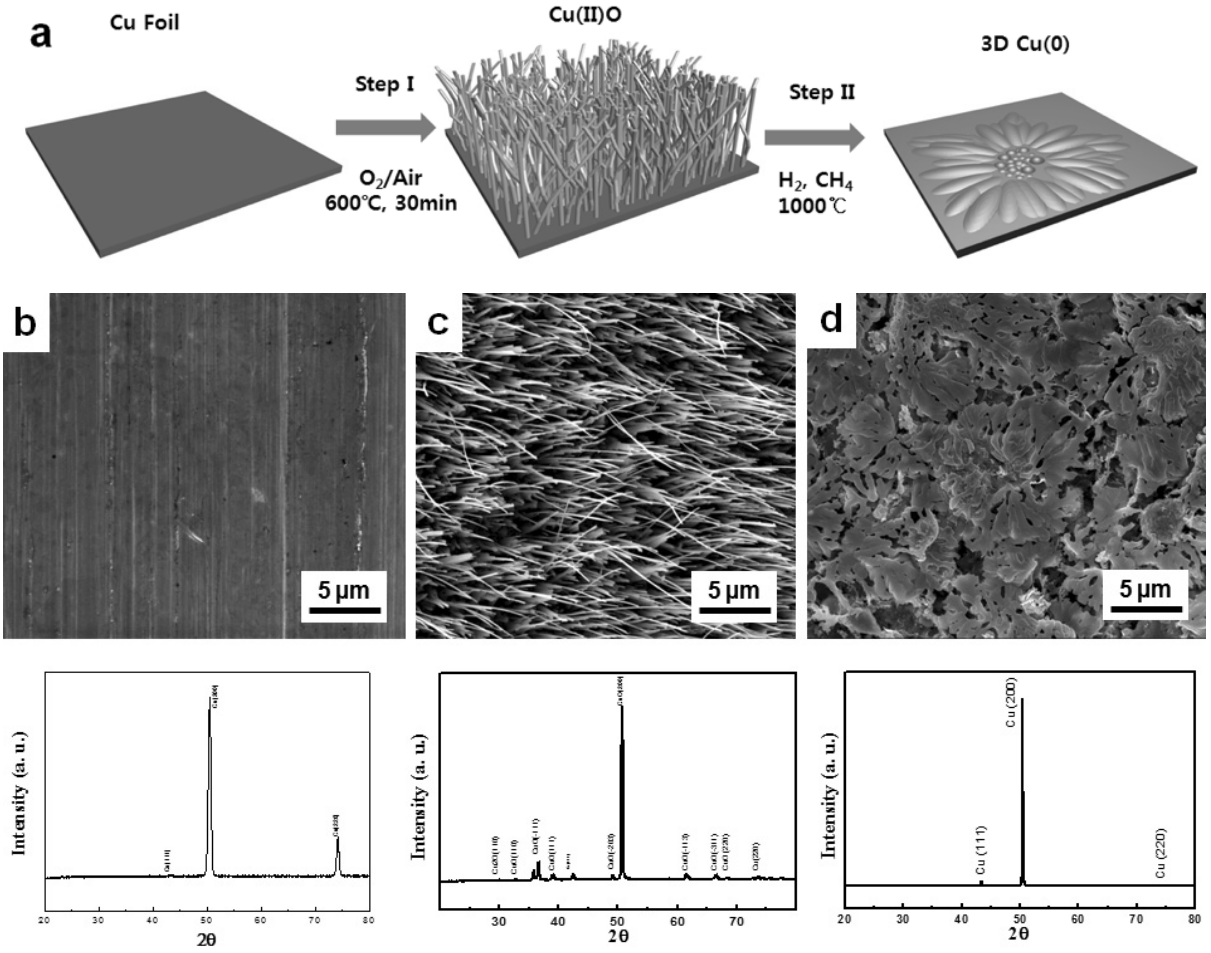


**Figure 17. Schematic description, SEM images, and XRD patterns of Cu, CuO, and reduced Cu created by self-assembly process of the surface during the heating and cooling steps: a) Schematic diagram of the oxidation/reduction cycle for the fabrication of CuO and 3D Cu. b-d) SEM images and corresponding XRD patterns below each SEM image of commerical copper foil (b), CuO nanowhiskers grown on a copper substrate under an oxygen enviroment (c), and reduced Cu upon diffusion of H2 at 1000 ºC (d).**

Nanostructures with a variety of shapes have potential applications in electronics and optoelectronics, since the morphology and the dimensions of structures are often directly related to the fundamental properties of the materials. For example, a rose-like 2D ZnO nanosheet has been developed to enhance the power conversion efficiency in dye-sensitized solar cells[19, 20], whereas flower-shaped 3D $MoS_2$ nanostructures[21, 22] exhibit excellent field emission properties due to the presence of open band edges in nanopetals. Therefore, preparation of multi-dimensionally ordered nanostructures with a variety of shapes is desirable in future material fabrication. We demonstrate here that various morphologies of 3D graphene structures having outstanding physicochemical properties can be generated simply by varying parameters for the oxidation of Cu and reduction of CuO. Figure 18 shows SEM images of graphene structures with various shapes grown by different processing conditions and the Raman spectrum taken from a representative CVD graphene sample on reduced Cu grown at 1000℃ and under $CH_4$/Ar gas. The growth of graphene initiated on the CuO 3D nano-frame starts immediately after the growth temperature of 1000℃ was reached and $CH_4$ was introduced into the chemical vapor deposition chamber. It is known that the graphene is nanostructured following the surface morphology of the underlying copper during the growth process. As a result, the CVD-grown graphene on the Cu frame has a distinctive 3D nature of the lateral dimension on the order of tens of micrometers, as shown in Figures 18(a)-18(c). The detailed conditions for the fabrication of 3D graphene structures with different morphologies, indicating shape tunability via our approach, are summarized. Briefly, experiments have shown that with a flatter surface of Cu, an accordingly smoother surface of graphene film can be obtained as the reduction temperature or duration of thermal processing time in an $H_2$ environment increases. This is because high temperature reduction of CuO causes significant collapse and coalescence of the newly formed neighboring sharp tips of Cu due to the much-lowered melting temperature of the nanoscale structure. Based on this finding, we could successfully tune the morphologies of 3D graphene from a nano-porous graphene structure (Figures 18(a) and 18(b)) to a flower-shaped large domain graphene film (Figure 18(c)) by simply changing the duration and the temperature for the reduction. Additionally, we observed that an oxidation process of CuO by dipping the Cu film in NaOH and $(NH_4)_2SO_5$ solutions for an hour before the thermal oxidation step promotes the realization of a surface with greatly enhanced and roughened morphologies. The Cu substrate is preoxidized by strong basic solutions in this process, thus facilitating a more twisted and porous surface in CuO nanostructures. For example, Figure 18(a) is a high resolution SEM image of graphene grown on a reduced Cu surface obtained from double oxidized CuO (solution + heat treatments). In contrast, Figure 18(b) shows the morphology of graphene surface with slightly decreased roughness, grown on Cu reduced from CuO created by a simple oxidation process (without peroxidation process) and treated under more severe reduction conditions. The morphology of Cu created by simple oxidation followed by thermal reduction for 30 min is typically a rose-like nanostructure with a substantially reduced morphology along the Cu surface, as shown in Figure 18(c). Figure 18(d) shows the Raman spectrum

of 3D graphene (sample 18(c)) grown on a 3D copper frame, confirmed from more than 10 different areas. The very small D band at 1350 $cm^{-1}$ indicates the absence of a significant number of defects of graphene at the edges despite the generation of many empty spaces in the 3D nanoframe. The G band at 1580 $cm^{-1}$ due to the doubly degenerate optical phonons of $E_{2g}$ symmetry and the very strong 2D band at 2700 $cm^{-1}$ confirms the high quality of constructed 3D graphene. The full-width-at-half-maximum (FWHM) is around 77 $cm^{-1}$. The low value of $I_D/I_G$, which is comparable to that of 2D graphene grown on commercial flat Cu (0.56), in particular implies reasonable quality of 3D graphene grown on the CuO nanoframe. In order to exploit the potential of 3D morphologies of graphene as a transparent electrode, we performed contact angel measurements. Figure 19 shows SEM images of a lotus leaf and lotus leaf-inspired graphene structure, and optical images of a water droplet on the surface of various substrates: three types of hydrophilic Cu substrates and three types of hydrophobic PDMS substrates. As shown in Figure 19(a), a lotus leaf is constructed with 10-20 um height and 10-15 um width papillaes, which are further textured by nanometer scale wrinkles.[23] The unusual superhydrophobicity and self-cleaning property of the lotus leaf is attributed to hierarchical micro-/nanostructures on the wax-coated low surface energy substrate. Therefore, we aimed at fabricating a dual scale (micro- and nano-) structure of graphene with a similar range of length-scales to those of the lotus leaf by controlling the oxidation and reduction conditions. Lotus leaf-like graphene is obtained when the processing conditions are intermediate between those for the samples in Figures 18(a) and 18(b). Figure 19(b) shows a SEM image of graphene with distinctive 3D nature of hierarchical bumps fabricated with conditions of 30 min oxidation at 500 $^oC$ under an air environment, reduction for 10 min, and 10 min duration at 850 $^oC$ by flowing 100/24 sccm of $H_2/CH_4$ gas under pressure of 4.0 torr. Figures 19 (c-e) show images of water droplets on three hydrophilic substrates: pristine Cu film (c), graphene/pristine Cu film (d), and as-prepared louts leaf-inspired graphene/Cu film (e). We confirm that the graphene films in both the 19(d) and (e) samples are single layer by Raman Spectra. Interestingly, despite the coverage of hydrophobic graphene film, the contact angle of the graphene/Cu film (d) does not show a noticeable increase relative to that of the pristine Cu film (c). This is because the atomic-scale thickness of the graphene film is not sufficiently able to amend the wettability of the Cu substrate, consistent with a previous report. However, compared to the contact angle of 79$^o$ of flat graphene on the pristine Cu film (d), the contact angle of the as-prepared lotus leaf-like graphene on the hydrophilic Cu substrate increases up to 110$^o$(e). Considering that the wettability of the surface is governed by two major factors, the roughness and low surface energy, along with the wetting transparency of our single layer graphene film, the excellent enhancement of the contact angle of the lotus leak-like graphene film on the hydrophilic Cu substrate is solely attributed to the 3D nature of the film. Figures 3f-3h compare the wettability of three different hydrophobic substrates.

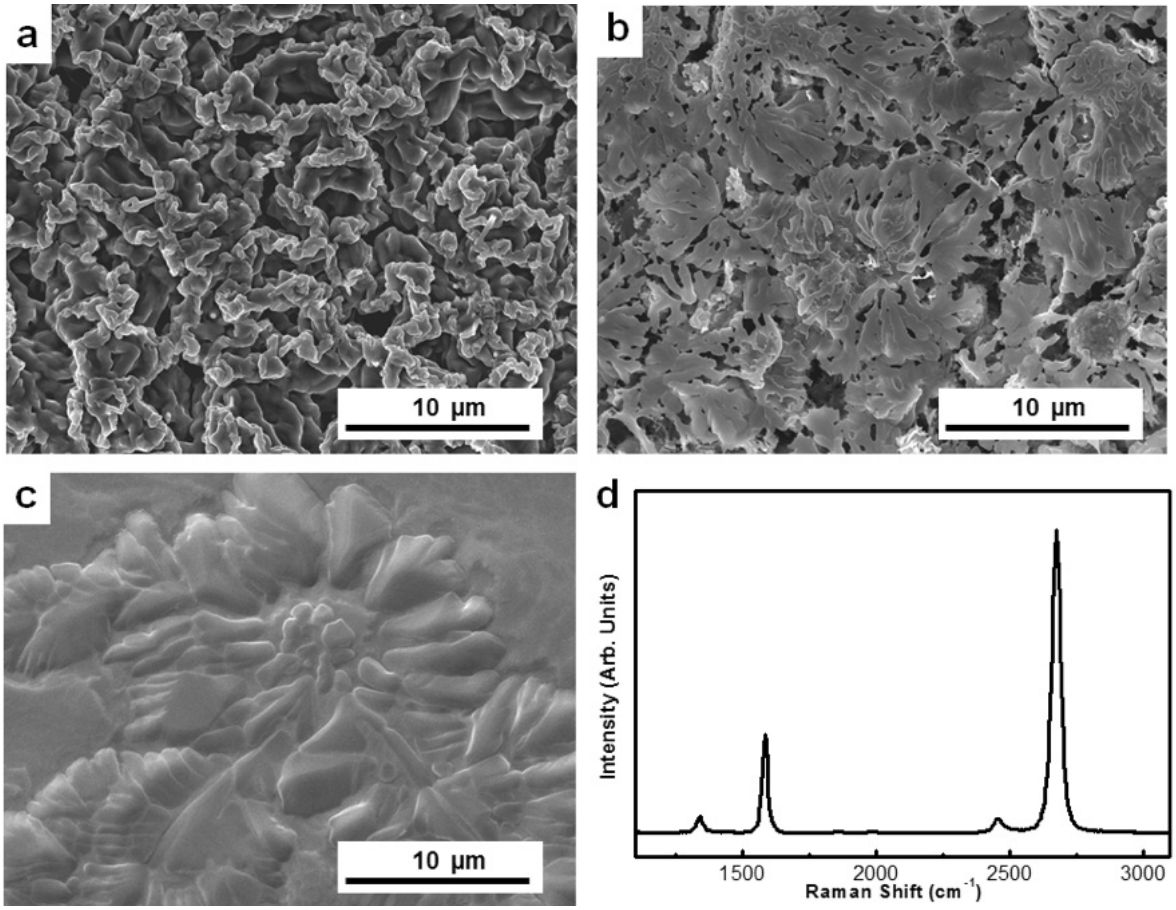


**Figure 18. SEM images of graphene grown by different oxidation and reduction parameters and Raman spectrum of graphene transferred on Si: Graphene grown by (a) 1hr annealing and 10 min growth at 850 oC on a double oxidized CuO substrate. (b) 1.5 hr annealing and 10 min growth at 900 oC on a normal CuO nanowhisker substrate. (c) 2hr annealing and 10 min growth at 1000 oC. (d) Raman spectrum of graphene grown by the conditions of (c) and transferred onto a silicon substrate.**

The contact angle of a water droplet on the 3D graphene surface on the PDMS substrate is as high as 170$^{o}$, much greater than that of the control sample (flat bare PDMS, **g**) (120 $^{o}$) and the lotus leaf (150$^{o}$). We observed that the surface of PDMS becomes hydrophilic after etching of Cu substrate in a NaOH solution for a day. In order to recover the original hydrophobicity of PDMS, we heated the control PDMS sample and the graphene coated PDMS sample on a hot plate overnight or treated the samples with silane. After heat treatment or chemical modification of the surface by the silane treatment, the surface of the lotus leaf-like graphene structure again became apparently superhydrophobic, with a contact angle of 170, whereas the corresponding values of PDMS are 150. Importantly, the 3D graphene retains the fundamental property of a reasonable sheet resistance of 400 Ω/□, which is adequate to be utilized as a hot wire, even with a curved shape and even after the silane treatment. This strongly suggests the possibility of realizing a superhydrophobic 3D graphene electrode on a flexible substrate.

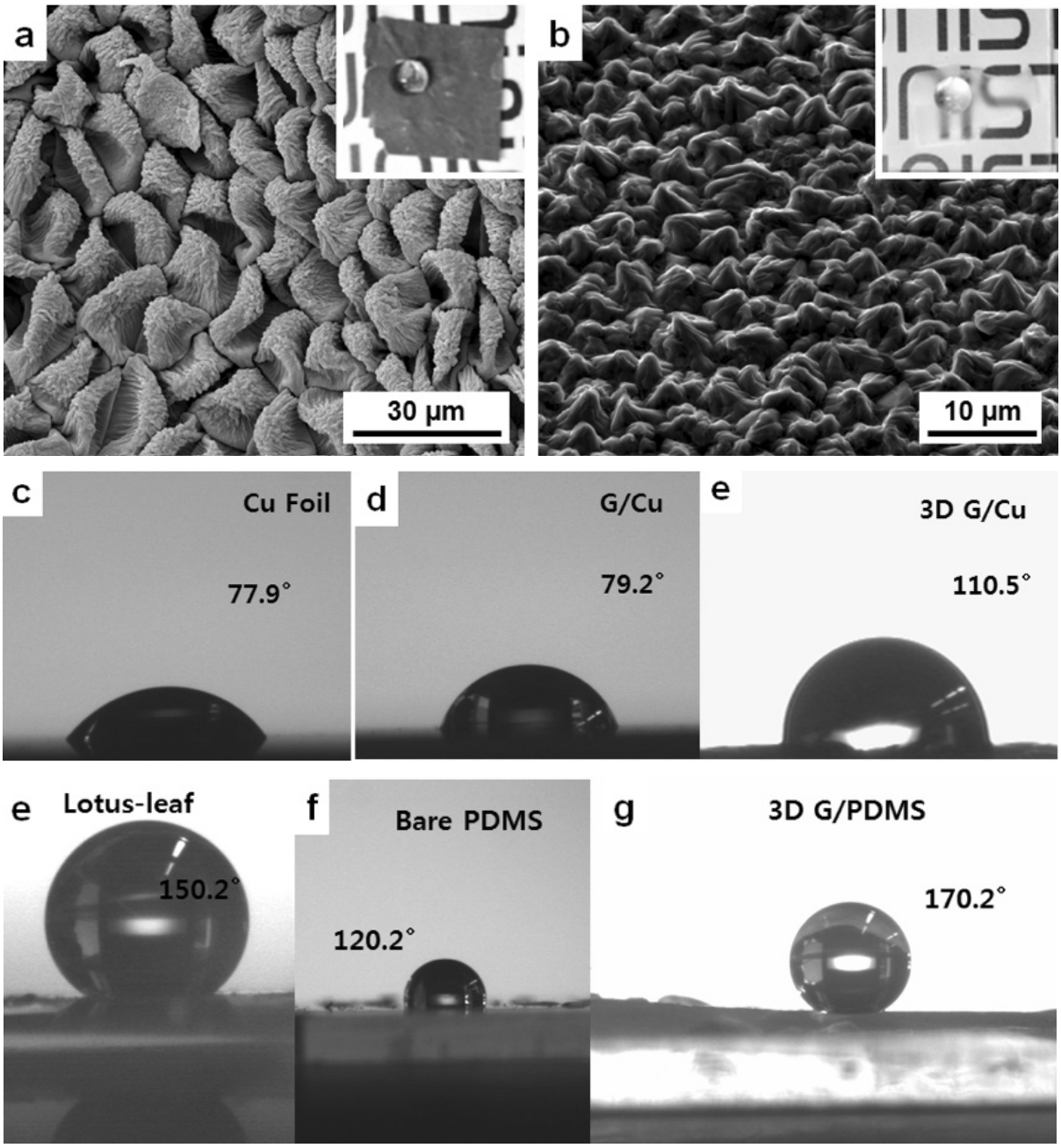


**Figure 19 : a-b) SEM image of the top surface of a lotus-leaf (a), and lotus leaf-inspired graphene grown on copper (b). In both cases, the inset is a photograph of a water droplet on each substrate, and the water droplet remains with very small contact on the substrate. The slight translucency of the film in the inset of figure 2b is due to the scattering of light caused by many pores in the 3D structure. c-d) Photograph of a water droplet on hydrophilic Cu (c), graphene/Cu surface (d), and lotus leaf inspired graphene/Cu surface (e). (f-h) Photograph of a water droplet on a lotus-leaf (f), on a plain hydrophobic PDMS (g), and on a 3D graphene/PDMS (h).**

### 4.4 Conclusions

we have created a lotus leaf-inspired 3D graphene electrode with water repellant properties via morphological change during the processes of oxidation of a flat Cu substrate and subsequent reduction of well-organized CuO under CVD growth conditions of graphene. The tailored synthesis of CuO and thus systematically reduced Cu with a surface morphology of double hierarchical bumps presents an ideal nucleation surface for various shapes of graphene, from rose-like rather flat graphene to lotus leaf-inspired 3D graphene structures. The contact angle of a water droplet on lotus leaf-inspired graphene reaches $170^{o}$, while the electrical resistance is as low as 400 Ω/sq. Our results suggest excellent capability of lotus leaf-like 3D graphene structures as electronic devices with both a super-hydrophobic property and electrical properties in large-scale production.

### 4.5 References


1. D. C. Elias, R. R. Nair, T. M. G. Mohiuddin, S. V. Morozov, P. Blake, M. P. Halsall, A. C. Ferrari, D. W. Boukhvalov, M. I. Katsnelson, A. K. Geim and K. S. Novoselov, *Science*, 2009, **323**, 610-613.
2. N. N. Klimov, S. Jung, S. Z. Zhu, T. Li, C. A. Wright, S. D. Solares, D. B. Newell, N. B. Zhitenev and J. A. Stroscio, *Science*, 2012, **336**, 1557-1561.
3. J. W. Suk, A. Kitt, C. W. Magnuson, Y. F. Hao, S. Ahmed, J. H. An, A. K. Swan, B. B. Goldberg and R. S. Ruoff, *Acs Nano*, 2011, **5**, 6916-6924.
4. Y. Wang, Y. Zheng, X. F. Xu, E. Dubuisson, Q. L. Bao, J. Lu and K. P. Loh, *Acs Nano*, 2011, **5**, 9927-9933.
5. M. Lafkioti, B. Krauss, T. Lohmann, U. Zschieschang, H. Klauk, K. von Klitzing and J. H. Smet, *Nano Lett*, 2010, **10**, 1149-1153.
6. H. Li and X. C. Zeng, *Acs Nano*, 2012, **6**, 2401-2409.
7. X. Q. Zhang, S. H. Wan, J. B. Pu, L. P. Wang and X. Q. Liu, *J Mater Chem*, 2011, **21**, 12251-12258.
8. Y. R. Lin, G. J. Ehlert, C. Bukowsky and H. A. Sodano, *Acs Appl Mater Inter*, 2011, **3**, 2200-2203.
9. J. Rafiee, M. A. Rafiee, Z. Z. Yu and N. Koratkar, *Advanced materials*, 2010, **22**, 2151-+.
10. S. H. Lee, H. W. Kim, J. O. Hwang, W. J. Lee, J. Kwon, C. W. Bielawski, R. S. Ruoff and S. O. Kim, *Angew Chem Int Edit*, 2010, **49**, 10084-10088.
11. X. C. Dong, J. Chen, Y. W. Ma, J. Wang, M. B. Chan-Park, X. M. Liu, L. H. Wang, W. Huang and P. Chen, *Chem Commun*, 2012, **48**, 10660-10662.
12. A. Ambrosi, A. Bonanni, Z. Sofer and M. Pumera, *Nanoscale*, 2013, **5**, 2379-2387.
13. M. Losurdo, M. M. Giangregorio, P. Capezzuto and G. Bruno, *Phys Chem Chem Phys*, 2011, **13**, 20836-20843.
14. J. Zhang, P. A. Hu, X. N. Wang, Z. L. Wang, D. Q. Liu, B. Yang and W. W. Cao, *J Mater Chem*, 2012, **22**, 18283-18290.
15. J. Rafiee, X. Mi, H. Gullapalli, A. V. Thomas, F. Yavari, Y. F. Shi, P. M. Ajayan and N. A. Koratkar, *Nat Mater*, 2012, **11**, 217-222.
16. F. Taherian, V. Marcon, N. F. A. van der Vegt and F. Leroy, *Langmuir*, 2013, **29**, 1457-1465.
17. A. Chaudhary and H. C. Barshilia, *J Phys Chem C*, 2011, **115**, 18213-18220.
18. X. C. Jiang, T. Herricks and Y. N. Xia, *Nano Lett*, 2002, **2**, 1333-1338.
19. J. P. Liu, X. T. Huang, Y. Y. Li, K. M. Sulieman, X. He and F. L. Sun, *J Mater Chem*, 2006, **16**, 4427-4434.
20. J. Y. Kim, J. A. Rodriguez, J. C. Hanson, A. I. Frenkel and P. L. Lee, *J Am Chem Soc*, 2003, **125**, 10684-10692.
21. F. Xu and L. T. Sun, *Energ Environ Sci*, 2011, **4**, 818-841.
22. Q. F. Zhang, C. S. Dandeneau, X. Y. Zhou and G. Z. Cao, *Advanced materials*, 2009, **21**, 4087-4108.
23. T. S. Li and G. L. Galli, *J Phys Chem C*, 2007, **111**, 16192-16196.
24. L. Ma, L. M. Xu, X. Y. Xu, Y. L. Luo and W. X. Chen, *Mater Lett*, 2009, **63**, 2022-2024.
25. H. J. Ensikat, P. Ditsche-Kuru, C. Neinhuis and W. Barthlott, *Beilstein J Nanotech*, 2011, **2**, 152-161.

**Publication list**


1. **Yoon, Jong-Chul**; Hwang, Jong-Ha; Thiyagarajan, Pradheep; Ruoff, Rodney; Jang, Ji-Hyun, Highly Enhanced Raman scattering on Carbonized Polymer Films, ACS Applied Materials & Interfaces, 2017.
2. **Jong-Chul Yoon**, Pradheep Thiyagarajan, Hyo-Jin Ahn, and Ji-Hyun Jang*, A Case Study: Effect of Defects in CVD-Grown Graphene on Graphene Enhanced Raman Spectroscopy, RCS advances, 2015.
3. **Jong-Chul Yoon**, Chang-Sung Yoon, Jung-Soo Lee, and Ji-Hyun Jang*, Lotus Leaf-Inspired CVD grown Graphene for a Water Repellant Flexible Transparent Electrode, Chemistry communication, 2013.
4. **Jong-Chul Yoon**, Jung-Soo Lee, Sun-I kim, Kwanghyun Kim, and Ji-Hyun Jang*, Three-Dimensional Graphene Nano-Networks with High Quality and Mass Production Capability via Precursor-Assisted Chemical Vapor Deposition, Scientific reports, 2013.
5. Jung-Soo Lee, **Jong-Chul Yoon**, and Ji-Hyun Jang*, A Route to Superhydrophobic Graphene Surfaces: Surface-Treated Reduced Graphene Oxide Spheres, JMC A.
6. Jung-Soo Lee, **Jong-Chul Yoon**, Pradheep Thiyagarajan, and Ji-Hyun Jang*, Graphene Oxide-Terminated Partially Fluorinated Poly(arylene ether sulfone), Chemistry Letters, 2012.
7. Hyo-Jin Ahn, Ik-Hee Kim, **Jong-Chul Yoon**, Sun-I Kim, and Ji-Hyun Jang*, p-Doped Three-Dimensional Graphene Nano-Networks Super to Platinum as a Counter Electrode for Dye-Sensitized Solar Cells, Chemical Communication, 2014.
8. Pradheep Thiyagarajan, Zhong Yan, **Jong-Chul Yoon**, Min-Wook Oh, and Ji-Hyun Jang*, Thermal Conductivity Reduction in Three-Dimensional Graphene-Based Nanofoam, RSC advances, 2015.
9. Jongha Hwang, Sun-I Kim, **Jong-Chul Yoon**, Seong-Ji Ha, and Ji-Hyun Jang*, "Realizing Battery-like Energy Density with Asymmetric Supercapacitors Achieved by Highly Conductive Three-Dimensional Graphene Current Collectors", JMA A, 2017.
10. Pradheep Thiyagarajan, Min-Wook Oh, **Jong-Chul Yoon**, and Ji-Hyun Jang*, Thermoelectric Properties of Nanoporous Three-Dimensional Graphene Networks, APL, 2014.
11. Sang-Ha Hwang, Hyo-Jin Ahn, **Jong-Chul Yoon**, Ji-Hyun Jang*, and Young-Bin Park*, Transparent Graphene Films with a Tunable Piezoresistvie Response, JMC C, 2013.

12. Jung-Soo Lee, Sun-I Kim, **Jong-Chul Yoon**, and Ji-Hyun Jang*, Chemical Vapor Deposition of Mesoporous Graphene Nanoballs for Supercapacitor, ACS Nano, 2013.
13. Hyo-Jin Ahn, Sun-I Kim, **Jong-Chul Yoon**, Jung-Soo Lee and Ji-Hyun Jang*, Power Conversion Efficiency Enhancement Based on the Bio-inspired Hierarchical Antireflection Layer in Dye Sensitized Solar Cells, Nanoscale, 2012.
14. Jung-Soo Lee, Hyo-Jin Ahn, **Jong-Chul Yoon** and Ji-Hyun Jang*, Three-Dimensional Nano-Foam of Few-Layer Graphene Grown by CVD for DSSC, PCCP, 2012.
15. Hyo-Jin Ahn, Pradheep Thiyagarajan, Lin Jia, Sun-I Kim, **Jong-Chul Yoon**, Edwin L. Thomas, and Ji-Hyun Jang*, An Optimal Substrate Design for SERS: Dual-Scale Diamond-Shaped Gold Nano-Structures Fabricated via Interference Lithography, nanoscale, 2013.
16. Pradheep Thiyagarajan, Hyo-Jin Ahn, Jung-Soo Lee, **Jong-Chul Yoon**, and Ji-Hyun Jang*, Hierarchical Metal/Semiconductor Nanostructure for Efficient Water Splitting, Small, 2013.

**Acknowledgment**

학부 시절을 거쳐 석사 과정을 마치는 지금까지의 과정을 되돌아보면 잘했던 것들과 부족했던 것들 그리고 잘못했던 것들이 떠오릅니다. 물리학이란 전공을 선택한 점, 조금의 정보도 없이 장지현 교수님 실험실에 지원을 하여 그래핀에 대해 연구를 한 것, 유니스트에 입학하게 된 것, 저에게 교수님과 함께 많은 가르침을 주었던 실험실 동료들 이 모든 것들은 저를 찬란하게 만듭니다. 여기까지 저를 이끌어주었던 장지현 교수님, 졸업한 선배 이정수 교수, 안효진 박사, 이명종 박사, 김선이 박사 그리고 앞으로도 계속 같이 연구하게 될 훌륭한 동료 김광현, 김성욱, 윤기용, 황종하, 곽명준, 박주형, 강경남, 민진욱, 강지훈, 하성지, 유선영, 안철원, 강세영, 이재은, 김수희 나를 보정해주고 미래의 안내판 역할을 해주며 많은 도움을 받았습니다. 특히 오랜 석사 과정의 마무리를 지을 수 있게 도와주신 장지현 교수님, 김진영 교수님 그리고 송현곤 교수님께 감사드립니다.

또 가까이 있지는 않지만 멀리서 서로 연락하며 지냈던 나의 친구들 제가 연구를 하며 지치거나 힘들 때 큰 버팀목이 되었고 고맙다고 전하고 싶습니다.

마지막으로 저를 가장 믿어주며 큰 의지가 되는 부모님과 나의 동생. 저의 바탕은 부모님과 동생입니다. 이 사실은 영원합니다. 그 튼튼한 기반을 바탕으로 여기까지 성장하였고 더 높아질 수 있습니다. 감사합니다. 또 하나의 마무리를 잘 지을 수 있도록 도와주셨던 수 많은 분들께 고마움을 표현합니다. 감사합니다.

수없이 반복되는 무더운 계절에

윤종철